

Observation of super-resolution in digital breast tomosynthesis

Raymond J. Acciavatti and Andrew D. A. Maidment

Citation: *Medical Physics* **39**, 7518 (2012); doi: 10.1118/1.4757583

View online: <http://dx.doi.org/10.1118/1.4757583>

View Table of Contents: <http://scitation.aip.org/content/aapm/journal/medphys/39/12?ver=pdfcov>

Published by the [American Association of Physicists in Medicine](#)

Articles you may be interested in

[A dual-view digital tomosynthesis imaging technique for improved chest imaging](#)

Med. Phys. **42**, 5238 (2015); 10.1118/1.4928214

[Oblique reconstructions in tomosynthesis. II. Super-resolution](#)

Med. Phys. **40**, 111912 (2013); 10.1118/1.4819942

[High resolution stationary digital breast tomosynthesis using distributed carbon nanotube x-ray source array](#)

Med. Phys. **39**, 2090 (2012); 10.1118/1.3694667

[A software-based x-ray scatter correction method for breast tomosynthesis](#)

Med. Phys. **38**, 6643 (2011); 10.1118/1.3659703

[The quantitative potential for breast tomosynthesis imaging](#)

Med. Phys. **37**, 1004 (2010); 10.1118/1.3285038

Educational Lectures

Don't miss these fascinating in-booth speakers. Lectures will be held throughout the show during exhibit hours only, in booth #4001.

Joe Ting, PhD

Utilizing EPID for stereotactic cone commissioning and verification in RIT

Sam Hancock, PhD

Isocenter optimization tools for LINAC-based SRS/SBRT

AAPM 2016 Learn and Earn



Users Meeting

Enjoy some delicious dessert while you learn and earn 2 CAMPEP credit hours at our Users Meeting.

Location . . . Marriott Marquis, Washington, DC

Date Sunday, July 31

Time 7-9 PM

Visit us
at AAPM
Booth #4001



call or visit
719.590.1077 • radimage.com

© 2016 RadImage Imaging Technology, Inc.
2016/1/6

Observation of super-resolution in digital breast tomosynthesis

Raymond J. Acciavatti and Andrew D. A. Maidment^{a)}

Department of Radiology, Perelman School of Medicine at the University of Pennsylvania, Philadelphia, Pennsylvania 19104-4206

(Received 4 March 2012; revised 14 September 2012; accepted for publication 14 September 2012; published 28 November 2012)

Purpose: Digital breast tomosynthesis (DBT) is a 3D x-ray imaging modality in which tomographic sections of the breast are generated from a limited range of tube angles. Because oblique x-ray incidence shifts the image of an object in subpixel detector element increments with each increasing projection angle, it is demonstrated that DBT is capable of super-resolution (i.e., subpixel resolution).

Methods: By convention, DBT reconstructions are performed on planes parallel to the breast support at various depths of the breast volume. In order for resolution in each reconstructed slice to be comparable to the detector, the pixel size should match that of the detector elements; hence, the highest frequency that can be resolved in the plane of reconstruction is the alias frequency of the detector. This study considers reconstruction grids with much smaller pixelation to visualize higher frequencies. For analytical proof of super-resolution, a theoretical framework is developed in which the reconstruction of a high frequency sinusoidal input is calculated using both simple backprojection (SBP) and filtered backprojection. To study the frequency spectrum of the reconstruction, its Fourier transform is also determined. The experimental feasibility of super-resolution was investigated by acquiring images of a bar pattern phantom with frequencies higher than the detector alias frequency.

Results: Using analytical modeling, it is shown that the central projection cannot resolve frequencies exceeding the detector alias frequency. The Fourier transform of the central projection is maximized at a lower frequency than the input as evidence of aliasing. By contrast, SBP reconstruction can resolve the input, and its Fourier transform is correctly maximized at the input frequency. Incorporating filters into the reconstruction smoothens pixelation artifacts in the spatial domain and reduces spectral leakage in the Fourier domain. It is also demonstrated that the existence of super-resolution is dependent on position in the reconstruction and on the directionality of the input frequency. Consistent with the analytical results, experimental reconstructions of bar patterns showed visibility of frequencies greater than the detector alias frequency. Super-resolution was present at positions predicted from analytical modeling.

Conclusions: This work demonstrates the existence of super-resolution in DBT. Super-resolution has the potential to impact the visualization of fine structural details in the breast, such as microcalcifications and other subtle signs of cancer. © 2012 American Association of Physicists in Medicine. [<http://dx.doi.org/10.1118/1.4757583>]

Key words: digital breast tomosynthesis (DBT), super-resolution, bar pattern phantom, microcalcifications, filtered backprojection (FBP)

I. INTRODUCTION

Digital breast tomosynthesis (DBT) is a 3D imaging modality in which low dose x-ray projections are acquired over a limited angular range about the breast. Using digital image reconstruction techniques, tomographic sections at all depths of the breast volume are subsequently generated. Unlike 2D digital mammography (DM), DBT can filter out overlapping anatomical structures which may hide a tumor. Preliminary studies indicate that DBT has greater sensitivity and specificity for cancer detection relative to DM.^{1,2}

In conventional practice, the reconstructed slices are generated on planes parallel to the breast support. In order to have the same in-plane resolution in the reconstruction as the detector, the pixel size in each reconstructed slice should match that of the detector elements. Using this approach, the highest frequency that can be resolved in the plane of

reconstruction is the alias frequency of the detector. This study considers the possibility for reconstruction grids with much smaller pixelation so that higher frequencies can be visualized. Because non-normal x-ray incidence causes the image of an object to be translated in subpixel detector element increments with each increasing projection angle, it is demonstrated in this work that DBT is capable of super-resolution (i.e., subpixel resolution).

Super-resolution has been well-described in a number of applications involving reconstruction from projections,³ including forensics, satellite imaging, computed tomography (CT), and magnetic resonance imaging (MRI); however, to our knowledge, its potential in DBT has not yet been demonstrated. An understanding of super-resolution and an analysis of how to optimize its presence may prove to be useful for designing the highest quality DBT systems. Although it is possible to improve spatial resolution simply by reducing the pixel

size of the detector, there are practical lower limits on the sizes that can be manufactured. In addition, one drawback of reducing the pixel size is decreasing the mean number of photons incident on each detector element and hence decreasing the signal-to-noise ratio (SNR) per pixel according to Poisson statistics⁴ for x-ray distributions. Clinically, super-resolution should be beneficial to diagnostic radiologists by improving the visibility of microcalcifications and other subtle signs of breast cancer with no increased radiation dose to the patient.

In this study, a theoretical framework for investigating super-resolution in DBT is developed by calculating the reconstruction of a sine input whose frequency is greater than the alias frequency of the detector. For optimal visualization of high frequencies in the 3D image, an infinitesimally fine (i.e., non-pixelated) reconstruction grid is considered. The reconstruction techniques include both simple backprojection (SBP) and filtered backprojection (FBP). In order to investigate the experimental feasibility of super-resolution using a commercial DBT system, images of a bar pattern phantom with frequencies higher than the alias frequency of the detector were acquired and subsequently reconstructed.

II. METHODS

II.A. Input object and acquisition geometry

An analytical framework for investigating the potential for super-resolution in DBT is now developed by calculating the reconstruction of a high frequency sinusoidal input.

Accordingly, suppose that a rectangular prism with infinite extent in the x and y directions has a linear attenuation coefficient $\mu(x, y, z)$ which varies sinusoidally along the x direction with frequency f_0 . Throughout the remainder of this paper, the input object will be termed a “sine plate.” With the xz plane defining the chest wall, the frequency vector is therefore oriented parallel to the chest wall side of the breast support. Figure 1 illustrates a cross section of the sine plate in the xz plane. As shown, the rectangular prism is positioned between $z = z_0 + \varepsilon/2$ and $z = z_0 - \varepsilon/2$, where z_0 is the central height of the prism and ε is the prism’s thickness. Defining the origin O as the midpoint of the chest wall side of the detector, the attenuation coefficient may be written as

$$\mu(x, y, z) = C \cdot \cos[2\pi f_0(x - x_0)] \cdot \text{rect}\left(\frac{z - z_0}{\varepsilon}\right), \quad (1)$$

where C is a constant denoting the amplitude of the waveform, x_0 is a translational shift in the waveform relative to the origin, and the rect function is defined by the expression

$$\text{rect}(u) \equiv \begin{cases} 1, & |u| \leq 1/2 \\ 0, & |u| > 1/2 \end{cases}. \quad (2)$$

By setting the amplitude C to $1/\varepsilon$, $\mu(x, y, z)$ may be normalized⁵ so that the total attenuation found by integrating along the z direction is simply $\cos[2\pi f_0(x - x_0)]$ for all ε . Provided that $|z - z_0| \leq \varepsilon$, the 1D Fourier transform (\mathcal{F}_1) of Eq. (1) along the x direction peaks at the frequencies $f_x = \pm f_0$, and vanishes at all other frequencies⁶

$$\mathcal{F}_1\mu(f_x, y, z) = \int_{-\infty}^{\infty} \mu(x, y, z) \cdot e^{-2\pi i f_x x} dx, \quad (3)$$

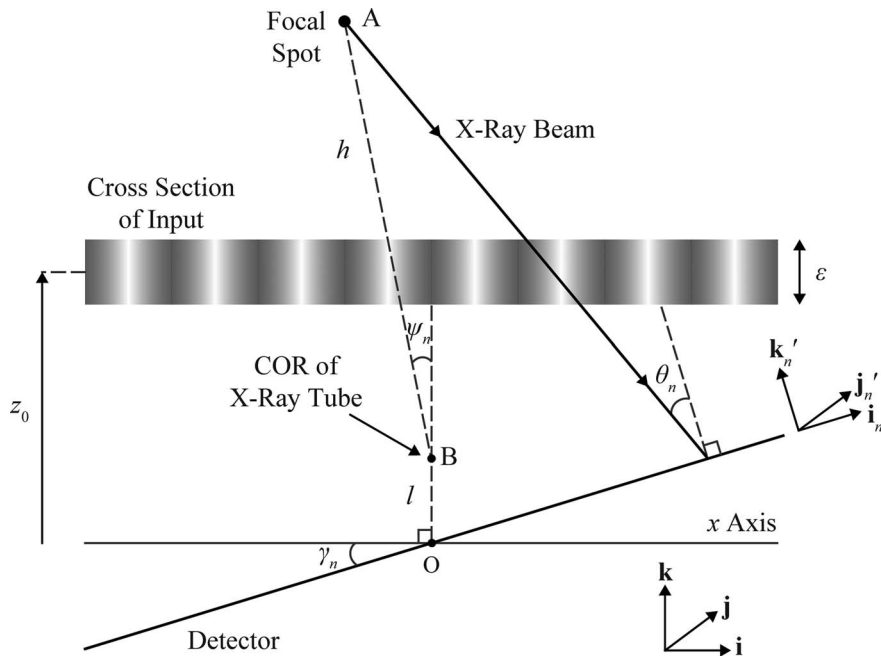


FIG. 1. The 3D input object is a rectangular prism whose linear attenuation coefficient varies sinusoidally with position x parallel to the chest wall side of the breast support. A 2D cross section of the input object through the plane of the chest wall is shown (figure not to scale). In acquiring projection images, the x-ray tube rotates within the xz plane about point B , and the detector simultaneously rotates about the y axis. The primed unit vectors \mathbf{i}'_n and \mathbf{j}'_n define the coordinate axes of the plane of the detector for the n th projection.

$$\begin{pmatrix} \mathbf{i}'_n \\ \mathbf{j}'_n \\ \mathbf{k}'_n \end{pmatrix} = \begin{pmatrix} \cos \gamma_n & 0 & \sin \gamma_n \\ 0 & 1 & 0 \\ -\sin \gamma_n & 0 & \cos \gamma_n \end{pmatrix} \begin{pmatrix} \mathbf{i} \\ \mathbf{j} \\ \mathbf{k} \end{pmatrix}. \quad (9)$$

Additional vectors from O to the COR at point B and from the COR to the focal spot at point A are

$$\vec{OB} = l\mathbf{k}, \quad (10)$$

$$\vec{BA} = (-h \sin \psi_n)\mathbf{i} + (h \cos \psi_n)\mathbf{k}, \quad (11)$$

where l is the COR-to-origin distance and where h is the source-to-COR distance. In Eq. (11), it is assumed that for positive values of ψ_n , the x coordinate of the focal spot at A is negative. This sign convention is chosen so that positive values of ψ_n cause the x component of the trajectory from A

to C to be positive for positive values of u_1 (Fig. 2). By the summation rules for vectors, the net vector from point C on the detector to the focal spot at A is

$$\vec{CA} = -\vec{OC} + \vec{OB} + \vec{BA}, \quad (12)$$

$$\begin{aligned} &= -(u_1 \cos \gamma_n + h \sin \psi_n)\mathbf{i} - u_2\mathbf{j} \\ &\quad + (l + h \cos \psi_n - u_1 \sin \gamma_n)\mathbf{k}. \end{aligned} \quad (13)$$

Thus, the angle of incidence is found from the expression

$$\cos \theta_n = \frac{\vec{CA} \cdot \mathbf{k}'_n}{|\vec{CA}| |\mathbf{k}'_n|}, \quad (14)$$

giving

$$\theta_n = \arccos \left[\frac{h \cos(\psi_n - \gamma_n) + l \cos \gamma_n}{\sqrt{(u_1 \cos \gamma_n + h \sin \psi_n)^2 + u_2^2 + (l + h \cos \psi_n - u_1 \sin \gamma_n)^2}} \right]. \quad (15)$$

The dot product in Eq. (14) has been computed using Eq. (9) to write \mathbf{k}'_n in terms of the unprimed unit vectors.

II.B. Detector signal

To calculate the detector signal for each projection, it is useful to perform ray tracing through the input object. We begin by defining the line from the focal spot at A to the incident point on the detector at C for the n th projection. This line can be expressed as the parametric equation

$$\begin{pmatrix} x \\ y \\ z \end{pmatrix} = w \begin{pmatrix} u_1 \cos \gamma_n + h \sin \psi_n \\ u_2 \\ u_1 \sin \gamma_n - l - h \cos \psi_n \end{pmatrix} + \begin{pmatrix} -h \sin \psi_n \\ 0 \\ l + h \cos \psi_n \end{pmatrix}, \quad (16)$$

where (x, y, z) is a point in \mathbb{R}^3 and w is a free parameter. The focal spot at A has been defined to correspond with $w = 0$, while the incident point at C has been defined to correspond with $w = 1$. The x-ray path length \mathcal{L}_n through the input object for the n th projection image is determined from the intersection of Eq. (16) with the planes $z = z_0 + \varepsilon/2$ and $z = z_0 - \varepsilon/2$. The values of w for these two points are

$$w_n^+ = \frac{z_0 + (\varepsilon/2) - l - h \cos \psi_n}{u_1 \sin \gamma_n - l - h \cos \psi_n}, \quad (17)$$

$$w_n^- = \frac{z_0 - (\varepsilon/2) - l - h \cos \psi_n}{u_1 \sin \gamma_n - l - h \cos \psi_n}, \quad (18)$$

where w_n^+ and w_n^- correspond to the entrance and exit points of the x-ray beam through the input, respectively. For the n th projection image, total x-ray attenuation $\mathcal{A}\mu(n)$ is now found by integrating $\mu(x, y, z)$ along \mathcal{L}_n

$$\mathcal{A}\mu(n) = \int_{\mathcal{L}_n} \mu ds. \quad (19)$$

The differential arc length ds along \mathcal{L}_n is

$$ds = \sqrt{\left(\frac{dx}{dw}\right)^2 + \left(\frac{dy}{dw}\right)^2 + \left(\frac{dz}{dw}\right)^2} dw, \quad (20)$$

$$= \sqrt{(u_1 \cos \gamma_n + h \sin \psi_n)^2 + u_2^2 + (l + h \cos \psi_n - u_1 \sin \gamma_n)^2} dw, \quad (21)$$

$$= [h \cos(\psi_n - \gamma_n) + l \cos \gamma_n] \sec(\theta_n) \cdot dw. \quad (22)$$

Equation (22) follows from Eq. (15). Substituting Eq. (22) into Eq. (19) yields the total x-ray attenuation

$$\mathcal{A}\mu(n) = \kappa_n \int_{w_n^+}^{w_n^-} \cos[2\pi f_0(u_1 \cos \gamma_n + h \sin \psi_n)w + \lambda_n] dw, \quad (23)$$

$$= \frac{\kappa_n (\sin [2\pi f_0(u_1 \cos \gamma_n + h \sin \psi_n)w_n^- + \lambda_n] - \sin [2\pi f_0(u_1 \cos \gamma_n + h \sin \psi_n)w_n^+ + \lambda_n])}{2\pi f_0(u_1 \cos \gamma_n + h \sin \psi_n)}, \quad (24)$$

where

$$\kappa_n = C[h \cos(\psi_n - \gamma_n) + l \cos \gamma_n] \sec \theta_n, \quad (25)$$

$$\lambda_n = -2\pi f_0(h \sin \psi_n + x_0). \quad (26)$$

Using a sum-to-product trigonometric identity for real numbers b_1 and b_2

$$\sin(b_1) - \sin(b_2) = 2 \cos\left(\frac{b_1 + b_2}{2}\right) \sin\left(\frac{b_1 - b_2}{2}\right), \quad (27)$$

one may rewrite Eq. (24) as

$$\mathcal{A}\mu(n) = \kappa_n(w_n^- - w_n^+) \cos[\pi f_0(u_1 \cos \gamma_n + h \sin \psi_n)(w_n^+ + w_n^-) + \lambda_n] \operatorname{sinc}\left[f_0(u_1 \cos \gamma_n + h \sin \psi_n)(w_n^- - w_n^+)\right], \quad (28)$$

$$= \frac{\varepsilon \kappa_n \cos\left[\frac{2\pi f_0(l + h \cos \psi_n - z_0)(u_1 \cos \gamma_n + h \sin \psi_n)}{l + h \cos \psi_n - u_1 \sin \gamma_n} + \lambda_n\right] \operatorname{sinc}\left[\frac{\varepsilon f_0(u_1 \cos \gamma_n + h \sin \psi_n)}{l + h \cos \psi_n - u_1 \sin \gamma_n}\right]}{l + h \cos \psi_n - u_1 \sin \gamma_n}, \quad (29)$$

where

$$\operatorname{sinc}(u) \equiv \frac{\sin(\pi u)}{\pi u}. \quad (30)$$

The transition from Eq. (28) to (29) follows from Eqs. (17) and (18). Equation (29) possesses a singularity at $u_1 = (l + h \cos \psi_n) \csc \gamma_n$, the point at which the denominator vanishes. For typical acquisition geometries, this singularity is not expected to correspond to a position on the detector, since neither the attenuation coefficient $\mu(x, y, z)$ nor the path length \mathcal{L}_n should have an infinity.

Equation (29) provides an expression for signal intensity versus position along the detector, assuming that the detector is non-pixelated and possesses an x-ray converter whose modulation transfer function (MTF) is unity at all frequencies. An amorphous selenium (*a*-Se) photoconductor operated in drift mode is a good approximation for an x-ray converter with these properties.⁷ In a clinical setting, *a*-Se is placed in contact with a plate of amorphous silicon (*a*-Si) in which a thin-film transistor (TFT) array samples detector signal in pixels (*i.e.*, detector elements).^{8–10} The logarithmically transformed signal in the \mathbf{m} th detector element for the n th projection is

$$\mathcal{D}\mu(\mathbf{m}, n) = \int_{a_y m_y}^{a_y(m_y+1)} \int_{a_x(m_x-1/2)}^{a_x(m_x+1/2)} \mathcal{A}\mu(n) \cdot \frac{du_1}{a_x} \frac{du_2}{a_y}. \quad (31)$$

In Eq. (31), m_x and m_y are integers used for labeling detector elements, and a_x and a_y denote detector element lengths in the directions parallel and perpendicular to the chest wall, respectively. In the special case of square detector elements, it is assumed that $a_x = a_y = a$. Detector elements are centered on $u_1 = m_x a_x$ and $u_2 = (m_y + 1/2)a_y$, where $m_x \in \mathbb{Z}$ and $m_y \in \mathbb{Z}^*$.

It is important to note that the integrand in Eq. (31) is dependent on both u_1 and u_2 due to the dependency of κ_n [Eq. (25)] on the incident angle θ_n [Eq. (15)]. However, because θ_n should vary minimally within the area of a single

detector element, total attenuation can be well approximated by the expression

$$\tilde{\mathcal{A}}\mu(n) = \mathcal{A}\mu(n)|_{\theta_n = \theta_{\mathbf{m}n}}, \quad (32)$$

where $\theta_{\mathbf{m}n}$ is the evaluation of θ_n at the centroid of the \mathbf{m} th detector element

$$\theta_{\mathbf{m}n} \equiv \theta_n|_{(u_1, u_2) = (m_x a_x, [m_y + 1/2] a_y)}, \quad (33)$$

so that

$$\mathcal{D}\mu(\mathbf{m}, n) \cong \int_{a_x(m_x-1/2)}^{a_x(m_x+1/2)} \tilde{\mathcal{A}}\mu(n) \cdot \frac{du_1}{a_x}. \quad (34)$$

Because it would be difficult to evaluate Eq. (34) in closed form, it is appropriate to apply approximate integration techniques. One such method is the midpoint formula¹¹

$$\mathcal{D}\mu(\mathbf{m}, n) \cong \lim_{J_x \rightarrow \infty} \frac{1}{J_x} \sum_{j_x=1}^{J_x} \tilde{\mathcal{A}}\mu(j_x, n), \quad (35)$$

where

$$\tilde{\mathcal{A}}\mu(j_x, n) \equiv \tilde{\mathcal{A}}\mu(n)|_{u_1 = a_x \left(\frac{j_x - 1/2}{J_x} + m_x - \frac{1}{2} \right)}. \quad (36)$$

The raw signal $\mathcal{S}\mu(u_1, u_2)$ across the detector can now be determined for the n th projection as

$$\begin{aligned} \mathcal{S}\mu(u_1, u_2) &= \sum_{\mathbf{m}} \mathcal{D}\mu(\mathbf{m}, n) \cdot \operatorname{rect}\left(\frac{u_1 - m_x a_x}{a_x}\right) \\ &\quad \cdot \operatorname{rect}\left(\frac{u_2 - (m_y + 1/2)a_y}{a_y}\right). \end{aligned} \quad (37)$$

Using this expression for raw signal, it is now possible to calculate the x-ray transform¹² $\mathcal{X}\mu(t_1, t_2)$

$$\begin{aligned} \mathcal{X}\mu(t_1, t_2) &= \sum_{\mathbf{m}} \mathcal{D}\mu(\mathbf{m}, n) \cdot \operatorname{rect}\left(\frac{t_1 \sec \theta_{\mathbf{m}n} - m_x a_x}{a_x}\right) \\ &\quad \cdot \operatorname{rect}\left(\frac{t_2 \sec \theta_{\mathbf{m}n} - (m_y + 1/2)a_y}{a_y}\right). \end{aligned} \quad (38)$$

To justify the transition from Eq. (37) to Eq. (38), one must determine the affine parameters t_1 and t_2 in terms of u_1 and u_2

by considering a line segment \overline{OD} which is orthogonal to \overline{AC} and which connects the origin with the x-ray beam (Fig. 2).

From trigonometry, the length $|\mathbf{t}| = \sqrt{t_1^2 + t_2^2}$ of \overline{OD} is

$$|\mathbf{t}| = |\mathbf{u}| \cos \theta_n. \quad (39)$$

By generalizing Eq. (39) to components, one finds $t_1 = u_1 \cos \theta_n$ and $t_2 = u_2 \cos \theta_n$. In Eq. (38), the incident angle across the area of the m th detector element for the n th projection has been approximated by its value at the centroid.

II.C. Filtered backprojection reconstruction from the projections

The reconstructed attenuation coefficient can now be determined by filtering the x-ray transform with the func-

tion $\phi(t_1, t_2)$ and backprojecting the result along the ray of incidence.¹³ It is customary to apply filtering exclusively to frequencies within the plane of the x-ray tube motion, so that the filter's 2D Fourier transform $\mathcal{F}_2\phi(f_1, f_2)$ is independent of f_2

$$\mathcal{F}_2\phi(f_1, f_2) = \mathcal{F}_1\phi(f_1), \quad (40)$$

and hence

$$\phi(t_1, t_2) = \phi(t_1)\delta(t_2). \quad (41)$$

The specific formula for $\phi(t_1)$ will be addressed in Sec II.D. Assuming that the reconstruction grid is infinitesimally fine (i.e., non-pixelated), the FBP reconstruction is

$$\mu_{\text{FBP}} = \sum_{\mathbf{m}, n} \frac{\mathcal{D}\mu(\mathbf{m}, n)}{N} \cdot \left[\phi(t_1) * \text{rect} \left(\frac{t_1 \sec \theta_{mn} - m_x a_x}{a_x} \right) \right] \Big|_{t_1 = x'_n \cos \theta_{mn} + z'_n \cos(\Gamma_{mn}) \sin(\theta_{mn})} \cdot \left[\text{rect} \left(\frac{t_2 \sec \theta_{mn} - (m_y + 1/2)a_y}{a_y} \right) \right] \Big|_{t_2 = y'_n \cos \theta_{mn} + z'_n \sin(\Gamma_{mn}) \sin(\theta_{mn})}, \quad (42)$$

where μ_{FBP} is the reconstructed attenuation coefficient and $*$ is the convolution operator. Within the plane of the detector, backprojection of signal in the m th detector element for the n th projection is directed azimuthally along the angle Γ_{mn} relative to the \mathbf{i}'_n axis (Fig. 2). As shown in Eq. (42), backprojection may be performed for each of the N projections using the primed coordinate system. To evaluate Eq. (42) at the point (x, y, z) in the unprimed coordinate system, one applies the matrix transformation given in Eq. (9).

It is now important to illustrate how the azimuthal backprojection angle Γ_{mn} is calculated. Begin by considering an arbitrary point E along the x-ray beam at which signal is backprojected from the incident point C (Fig. 2). A line segment along the \mathbf{k}'_n direction may then be drawn from E to the point F on the detector for the n th projection. As a result, within the plane of the detector, backprojection is directed from C to F at the angle Γ_n relative to the \mathbf{i}'_n axis. Point G may now be defined as the position at the chest wall side of the detector which is collinear with points C and F. A derivation of the formula for Γ_n requires knowledge of the distance d_n between G and O, which is now calculated

$$\overrightarrow{GO} = d_n \mathbf{i}'_n, \quad (43)$$

$$= (d_n \cos \gamma_n) \mathbf{i} + (d_n \sin \gamma_n) \mathbf{k}. \quad (44)$$

Since ACG and ECF are similar triangles, \overrightarrow{GA} is parallel to \overrightarrow{FE} and is in turn parallel to \mathbf{k}'_n . Denoting \times as the cross product operator, it follows that:

$$\overrightarrow{GA} \times \mathbf{k}'_n = \mathbf{0}, \quad (45)$$

where

$$\overrightarrow{GA} = \overrightarrow{GO} + \overrightarrow{OA}, \quad (46)$$

$$= (d_n \cos \gamma_n - h \sin \psi_n) \mathbf{i} + (d_n \sin \gamma_n + l + h \cos \psi_n) \mathbf{k}. \quad (47)$$

To calculate \overrightarrow{OA} in Eq. (46), Eqs. (10) and (11) have been summed. Substituting Eqs. (9) and (47) into the cross product of Eq. (45) gives

$$\overrightarrow{GA} \times \mathbf{k}'_n = \begin{vmatrix} \mathbf{i} & \mathbf{j} & \mathbf{k} \\ d_n \cos \gamma_n - h \sin \psi_n & 0 & d_n \sin \gamma_n + l + h \cos \psi_n \\ -\sin \gamma_n & 0 & \cos \gamma_n \end{vmatrix}, \quad (48)$$

$$= -[d_n + l \sin \gamma_n - h \sin(\psi_n - \gamma_n)] \mathbf{j}. \quad (49)$$

By combining Eqs. (45) and (49), one can solve for d_n

$$d_n = h \sin(\psi_n - \gamma_n) - l \sin \gamma_n. \quad (50)$$

Using this result, it follows from trigonometry that

$$\cos \Gamma_n = \frac{u_1 + d_n}{\sqrt{(u_1 + d_n)^2 + u_2^2}}, \quad (51)$$

$$\sin \Gamma_n = \frac{u_2}{\sqrt{(u_1 + d_n)^2 + u_2^2}}. \quad (52)$$

Substituting the coordinates of the detector element centroid into Eqs. (51) and (52), one finds that the azimuthal backprojection angle for the m th detector element in the n th projection satisfies the properties

$$\cos \Gamma_{mn} = \frac{m_x a_x + d_n}{\sqrt{(m_x a_x + d_n)^2 + (m_y + 1/2)^2 a_y^2}}, \tag{53}$$

$$\sin \Gamma_{mn} = \frac{(m_y + 1/2) a_y}{\sqrt{(m_x a_x + d_n)^2 + (m_y + 1/2)^2 a_y^2}}. \tag{54}$$

These relations are the expressions needed for FBP reconstruction in Eq. (42). One special case of Eq. (42) is SBP reconstruction

$$\begin{aligned} \mathcal{B}(\mathcal{X}\mu) = & \sum_{\mathbf{m},n} \frac{\mathcal{D}\mu(\mathbf{m}, n)}{N} \\ & \cdot \text{rect} \left(\frac{x'_n + z'_n \cos(\Gamma_{mn}) \tan(\theta_{mn}) - m_x a_x}{a_x} \right) \\ & \cdot \text{rect} \left(\frac{y'_n + z'_n \sin(\Gamma_{mn}) \tan(\theta_{mn}) - (m_y + 1/2) a_y}{a_y} \right), \end{aligned} \tag{55}$$

where \mathcal{B} denotes the backprojection operator. With SBP, the filter $\phi(t_1, t_2)$ effectively becomes the product $\delta(t_1)\delta(t_2)$.

According to Eq. (55), backprojection in the primed coordinate system occurs by translating x'_n and y'_n by $-z'_n \cos(\Gamma_{mn}) \tan(\theta_{mn})$ and $-z'_n \sin(\Gamma_{mn}) \tan(\theta_{mn})$, respectively, where z'_n is the height of the backprojected point (E) above the plane of the detector. These translational shifts are illustrated in Fig. 2.

II.D. Formulation of the reconstruction filter

Following Zhao’s linear systems theory for DBT,¹⁴ a ramp (RA) filter should be applied to the x-ray transform of each projection to reduce the low frequency detector response.¹⁵ The filter is truncated at the spatial frequencies $f_1 = -\xi$ and $f_1 = +\xi$ in the Fourier domain

$$\mathcal{F}_1 \phi_{\text{RA}}(f_1) = \begin{cases} |f_1|, & |f_1| \leq \xi \\ 0, & |f_1| > \xi \end{cases}. \tag{56}$$

The spatial representation $\phi_{\text{RA}}(t_1)$ of the RA filter is determined by its inverse Fourier transform⁶

$$\phi_{\text{RA}}(t_1) = \int_{-\infty}^{\infty} \mathcal{F}_1 \phi_{\text{RA}}(f_1) \cdot e^{2\pi i t_1 f_1} df_1, \tag{57}$$

$$= \xi^2 [2\text{sinc}(2\xi t_1) - \text{sinc}^2(\xi t_1)]. \tag{58}$$

Using this result, the convolution in Eq. (42) can be calculated

$$\phi_{\text{RA}}(t_1) * \text{rect} \left(\frac{t_1 \sec \theta_{mn} - m_x a_x}{a_x} \right) = \frac{\left[a_x \cos(\theta_{mn}) [\cos(\pi a_x \xi \cos \theta_{mn}) \cos [2\pi \xi (t_1 - m_x a_x \cos \theta_{mn})] - 1] + 2(t_1 - m_x a_x \cos \theta_{mn}) \sin(\pi a_x \xi \cos \theta_{mn}) \sin [2\pi \xi (t_1 - m_x a_x \cos \theta_{mn})] \right]}{2\pi^2 [t_1 - (m_x - 1/2) a_x \cos \theta_{mn}] [t_1 - (m_x + 1/2) a_x \cos \theta_{mn}]}. \tag{59}$$

Since noise tends to occur at high frequencies, a spectrum apodization (SA) filter is often applied in addition to the RA filter in order to reduce the high frequency detector response. Following Zhao’s approach, a Hanning window function is the SA filter

$$\mathcal{F}_1 \phi_{\text{SA}}(f_1) = \begin{cases} \frac{1}{2} \left[1 + \cos \left(\frac{\pi f_1}{\xi} \right) \right], & |f_1| \leq \xi \\ 0, & |f_1| > \xi \end{cases}, \tag{60}$$

$$\phi_{\text{SA}}(t_1) = \frac{\xi \text{sinc}(2\xi t_1)}{1 - 4\xi^2 t_1^2}. \tag{61}$$

According to the convolution theorem,⁶ the net filter is thus

$$\phi_{\text{SA}}(t_1) * \phi_{\text{RA}}(t_1) = \frac{\xi^2 [\pi^2 (12\xi^2 t_1^2 - 1) \text{sinc}^2(\xi t_1) - 2\pi^2 (4\xi^2 t_1^2 - 1) \text{sinc}(2\xi t_1) - 4(4\xi^2 t_1^2 + 1)]}{2\pi^2 (4\xi^2 t_1^2 - 1)^2}. \tag{62}$$

The convolution of the net filter in Eq. (62) with the rect function in Eq. (42) can be performed in closed form similar to Eq. (59). This expression is omitted as it is lengthy.

II.E. Fourier transform of the DBT images

According to Eq. (4), the Fourier transform of the input along the x direction peaks at the frequencies $f_x = \pm f_0$. To determine whether the frequency spectra of the DBT images possess this expected dependency on f_0 , their continuous Fourier transforms may be considered. Within the plane of the

detector, the 2D Fourier transform of the n th projection is

$$\begin{aligned} \mathcal{F}_2(\mathcal{S}\mu)(f_1, f_2) &= \int_{-\infty}^{\infty} \int_{-\infty}^{\infty} \mathcal{S}\mu(u_1, u_2) \\ &\cdot e^{-2\pi i (f_1 u_1 + f_2 u_2)} du_1 du_2, \end{aligned} \tag{63}$$

$$= a_x a_y \cdot \text{sinc}(a_x f_1) \text{sinc}(a_y f_2) \cdot \sum_{\mathbf{m}} \mathcal{D}\mu(\mathbf{m}, n) \cdot e^{-2\pi i [m_x a_x f_1 + (m_y + 1/2) a_y f_2]} \quad (64)$$

The 2D Fourier transform of the reconstruction along the x and y directions may now be calculated by considering a fixed height z . Because this study only considers input frequencies parallel to the xy plane, it is unnecessary to transform along the z direction. Although filtered backprojection reconstruction in Eq. (42) is performed in the primed coordinate system, it is important to take the Fourier transform in the unprimed coordinate system. As such, the reconstructed attenuation coefficient can be written in the form

$$\mu_{\text{FBP}}(x, y, z) = \sum_{\mathbf{m}, n} \frac{\mathcal{D}\mu(\mathbf{m}, n)}{N} \cdot [\rho_1(t_1)]|_{t_1=\sigma_{1mn}x+\sigma_{2mn}z} \cdot [\rho_2(t_2)]|_{t_2=\sigma_{3mn}x+\sigma_{4mn}y+\sigma_{5mn}z}, \quad (65)$$

where

$$\rho_1(t_1) = \phi(t_1) * \text{rect}\left(\frac{t_1 \sec \theta_{mn} - m_x a_x}{a_x}\right), \quad (66)$$

$$\rho_2(t_2) = \text{rect}\left(\frac{t_2 \sec \theta_{mn} - (m_y + 1/2) a_y}{a_y}\right), \quad (67)$$

and

$$\sigma_{1mn} = \cos(\gamma_n) \cos(\theta_{mn}) - \cos(\Gamma_{mn}) \sin(\gamma_n) \sin(\theta_{mn}), \quad (68)$$

$$\sigma_{2mn} = \sin(\gamma_n) \cos(\theta_{mn}) + \cos(\Gamma_{mn}) \cos(\gamma_n) \sin(\theta_{mn}), \quad (69)$$

$$\sigma_{3mn} = -\sin(\Gamma_{mn}) \sin(\gamma_n) \sin(\theta_{mn}), \quad (70)$$

$$\sigma_{4mn} = \cos \theta_{mn}, \quad (71)$$

$$\sigma_{5mn} = \sin(\Gamma_{mn}) \cos(\gamma_n) \sin(\theta_{mn}). \quad (72)$$

According to the convolution theorem, the Fourier transform of Eq. (66) under the frequency variable f_1 is

$$\mathcal{F}_1 \rho_1(f_1) = \mathcal{F}_1 \phi(f_1) \cdot a_x \cos(\theta_{mn}) \text{sinc}(a_x f_1 \cos \theta_{mn}) \cdot e^{-2\pi i m_x a_x f_1 \cos \theta_{mn}}. \quad (73)$$

In the special case of SBP reconstruction, the filter in Eq. (73) is unity. In a similar fashion, the Fourier transform of Eq. (67) may be written

$$\mathcal{F}_1 \rho_2(f_2) = a_y \cos(\theta_{mn}) \text{sinc}(a_y f_2 \cos \theta_{mn}) \cdot e^{-2\pi i (m_y + 1/2) a_y f_2 \cos \theta_{mn}}. \quad (74)$$

The 2D Fourier transform of Eq. (65) at the fixed depth z is now determined from the expression

$$\mathcal{F}_2 \mu_{\text{FBP}}(f_x, f_y, z) = \sum_{\mathbf{m}, n} \frac{\mathcal{D}\mu(\mathbf{m}, n)}{N} \cdot \int_{-\infty}^{\infty} \rho_1(\sigma_{1mn}x + \sigma_{2mn}z) \cdot I_{y\mathbf{m}n}(x) \cdot e^{-2\pi i f_x x} dx, \quad (75)$$

where $I_{y\mathbf{m}n}(x)$ is given by the integral

$$I_{y\mathbf{m}n}(x) = \int_{-\infty}^{\infty} \rho_2(\sigma_{3mn}x + \sigma_{4mn}y + \sigma_{5mn}z) \cdot e^{-2\pi i f_y y} dy. \quad (76)$$

To evaluate Eq. (76), one can make the change of variables $\eta_{y\mathbf{m}n} = \sigma_{3mn}x + \sigma_{4mn}y + \sigma_{5mn}z$. Since $\sigma_{4mn} > 0$, it follows that:

$$I_{y\mathbf{m}n}(x) = \int_{-\infty}^{\infty} \rho_2(\eta_{y\mathbf{m}n}) e^{\frac{-2\pi i f_y (\eta_{y\mathbf{m}n} - \sigma_{3mn}x - \sigma_{5mn}z)}{\sigma_{4mn}}} \frac{d\eta_{y\mathbf{m}n}}{\sigma_{4mn}}, \quad (77)$$

$$= \frac{e^{\frac{2\pi i f_y (\sigma_{3mn}x + \sigma_{5mn}z)}{\sigma_{4mn}}}}{\sigma_{4mn}} \int_{-\infty}^{\infty} \rho_2(\eta_{y\mathbf{m}n}) \cdot e^{-2\pi i \left(\frac{f_y}{\sigma_{4mn}}\right) \eta_{y\mathbf{m}n}} d\eta_{y\mathbf{m}n}, \quad (78)$$

$$= \frac{e^{\frac{2\pi i f_y (\sigma_{3mn}x + \sigma_{5mn}z)}{\sigma_{4mn}}}}{\sigma_{4mn}} \mathcal{F}_1 \rho_2\left(\frac{f_y}{\sigma_{4mn}}\right), \quad (79)$$

where $\mathcal{F}_1 \rho_2$ has been previously calculated in Eq. (74). Using Eq. (79), Eq. (75) can now be rewritten as

$$\mathcal{F}_2 \mu_{\text{FBP}}(f_x, f_y, z) = \sum_{\mathbf{m}, n} \frac{\mathcal{D}\mu(\mathbf{m}, n)}{N} \frac{e^{\frac{2\pi i f_y \sigma_{5mn} z}{\sigma_{4mn}}} I_{x\mathbf{m}n}}{\sigma_{4mn}} \mathcal{F}_1 \rho_2\left(\frac{f_y}{\sigma_{4mn}}\right), \quad (80)$$

where

$$I_{x\mathbf{m}n} = \int_{-\infty}^{\infty} \rho_1(\sigma_{1mn}x + \sigma_{2mn}z) e^{-2\pi i \left(f_x - \frac{\sigma_{3mn} f_y}{\sigma_{4mn}}\right) x} dx. \quad (81)$$

To evaluate Eq. (81), it is helpful to perform the substitution $\eta_{x\mathbf{m}n} = \sigma_{1mn}x + \sigma_{2mn}z$,

$$I_{x\mathbf{m}n} = \int_{-\infty}^{\infty} \rho_1(\eta_{x\mathbf{m}n}) e^{-2\pi i \left(f_x - \frac{\sigma_{3mn} f_y}{\sigma_{4mn}}\right) \left(\frac{\eta_{x\mathbf{m}n} - \sigma_{2mn} z}{\sigma_{1mn}}\right)} \frac{d\eta_{x\mathbf{m}n}}{|\sigma_{1mn}|}, \quad (82)$$

$$= \frac{e^{\frac{2\pi i \sigma_{2mn} z (\sigma_{4mn} f_x - \sigma_{3mn} f_y)}{\sigma_{1mn} \sigma_{4mn}}}}{|\sigma_{1mn}|} \int_{-\infty}^{\infty} \rho_1(\eta_{x\mathbf{m}n}) \cdot e^{-2\pi i \left(\frac{\sigma_{4mn} f_x - \sigma_{3mn} f_y}{\sigma_{1mn} \sigma_{4mn}}\right) \eta_{x\mathbf{m}n}} d\eta_{x\mathbf{m}n}, \quad (83)$$

$$= \frac{e^{\frac{2\pi i \sigma_{2mn} z (\sigma_{4mn} f_x - \sigma_{3mn} f_y)}{\sigma_{1mn} \sigma_{4mn}}}}{|\sigma_{1mn}|} \mathcal{F}_1 \rho_1\left(\frac{\sigma_{4mn} f_x - \sigma_{3mn} f_y}{\sigma_{1mn} \sigma_{4mn}}\right), \quad (84)$$

where $\mathcal{F}_1 \rho_1$ is given by Eq. (73). The final expression for the 2D Fourier transform of the reconstruction can now be derived by combining Eqs. (80) and (84)

$$\mathcal{F}_2 \mu_{\text{FBP}}(f_x, f_y, z) = \sum_{\mathbf{m}, n} \frac{\mathcal{D}\mu(\mathbf{m}, n)}{N} \frac{e^{\frac{2\pi i z}{\sigma_{1mn}\sigma_{4mn}} [\sigma_{2mn}\sigma_{4mn} f_x + (\sigma_{1mn}\sigma_{5mn} - \sigma_{2mn}\sigma_{3mn}) f_y]}}{|\sigma_{1mn}| \sigma_{4mn}} \mathcal{F}_1 \rho_1 \left(\frac{\sigma_{4mn} f_x - \sigma_{3mn} f_y}{\sigma_{1mn}\sigma_{4mn}} \right) \mathcal{F}_1 \rho_2 \left(\frac{f_y}{\sigma_{4mn}} \right). \quad (85)$$

A special case of this result is important to consider

$$\begin{aligned} \mathcal{F}_2 \mu_{\text{FBP}}(f_x, 0, z) \\ = \sum_{\mathbf{m}, n} \frac{\mathcal{D}\mu(\mathbf{m}, n)}{N} \frac{e^{\frac{2\pi i \sigma_{2mn} z f_x}{\sigma_{1mn}}} a_y \cos \theta_{mn}}{|\sigma_{1mn}| \sigma_{4mn}} \mathcal{F}_1 \rho_1 \left(\frac{f_x}{\sigma_{1mn}} \right). \end{aligned} \quad (86)$$

Equation (86) is useful for analyzing the reconstruction of an input frequency oriented along the x direction; that is, $f_y = 0$.

III. THEORETICAL RESULTS

III.A. Input frequency directed parallel to the chest wall side of the breast support

Image acquisition is now simulated for a Selenia Dimensions integrated multimode mammography and tomosynthesis x-ray system (Hologic Inc., Bedford, MA) having 15 projections, an angular spacing ($\Delta\psi$) of 1.07° between projections, a source-to-COR distance (h) of 70.0 cm, a COR-to-origin distance (l) of 0 cm, and square detector element length ($a_x = a_y = a$) of $140 \mu\text{m}$. In addition, the sine plate has a thickness (ϵ) of 0.5 mm, a translational shift (x_0) of 0 mm along the direction of the chest wall side of the breast support, and a frequency (f_0) of $0.7a^{-1}$ (5.00 lp/mm) parallel to the x axis. To illustrate the potential for super-resolution in DBT, the input frequency is chosen to be higher than the detector alias frequency $0.5a^{-1}$ (3.57 lp/mm). The sine plate is placed at a depth corresponding to the mid-thickness of a typical breast size (50.0 mm thick) under compression. With the breast support positioned 25.0 mm above the origin of the detector, the sine plate is therefore positioned at the depth $z_0 = 50.0$ mm.

FBP reconstructions are performed with either the RA filter alone or the RA and SA filters together, assuming a truncation frequency (ξ) of $2a^{-1}$ (14.3 lp/mm). Although ξ is typically chosen to be the detector alias frequency $0.5a^{-1}$, it is necessary to choose a higher value to achieve super-resolution. The specified value of ξ corresponds to the second zero of the MTF of the detector sampling process for frequency measurements along the f_1 direction ($f_2 = 0$)^{16–18}

$$\text{MTF}(f_1, f_2) = \text{sinc}(a_x f_1) \text{sinc}(a_y f_2). \quad (87)$$

Figure 3 shows a plot of the reconstruction filters versus frequency. The two filters almost perfectly match each other at low frequencies but diverge at high frequencies, since the SA filter is intended to suppress high frequency noise.

III.A.1. Individual projections

At a fixed distance (u_2) of 30.0 mm from the chest wall, Figs. 4(a) and 4(b) show a cross section of signal versus detector position u_1 for the central projection ($n = 0$) and an oblique projection ($n = 7$) of the sine plate. The u_2 displacement lies between the chest wall and nipple of a typical breast. In the recent development of a physical 3D anthropomorphic phantom for image quality assessment in DM and DBT,^{19,20} Carton *et al.* modeled a distance of 65.0 mm between the chest wall and nipple for an average breast size of 450 ml. The u_2 displacement considered in Figs. 4(a) and 4(b) thus corresponds to a position approximately halfway between the chest wall and nipple of this phantom.

Detector signal is a discrete function [Eq. (31)] due to detector element sampling. To represent this signal graphically, the presence of each detector element can be modeled by a rectangle function, so that the projections appear to be step-like in Figs. 4(a) and 4(b). The width of each step matches the detector element length ($140 \mu\text{m}$).

In Figs. 4(c) and 4(d), the modulus of the Fourier transform of detector signal is plotted versus frequency f_1 , assuming $f_2 = 0$ [Eq. (64)]. The central and oblique projections are similar in that they both represent a high frequency input as if it were a lower frequency. The major peak of the Fourier transform of either projection does not occur at the input frequency 5.00 lp/mm but instead occurs at a lower frequency as evidence of aliasing.

The two projections and their frequency spectra are also plotted in Fig. 4 for an infinite source-to-COR distance (h) with no other changes in the acquisition parameters. This limiting case transforms the divergent beam geometry into a parallel beam geometry. Consequently, the x-ray angle relative to the normal to the detector does not vary with

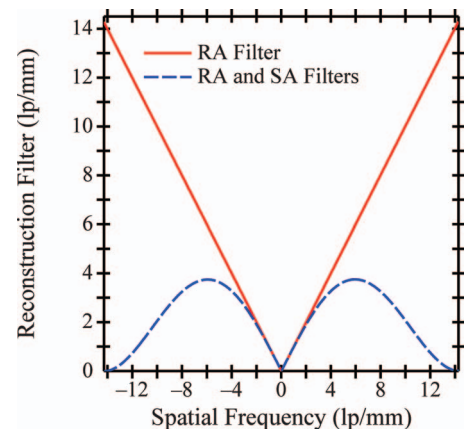


FIG. 3. Reconstruction is performed with either the ramp (RA) filter alone or the RA and spectrum apodization (SA) filters together. The SA filter is a Hanning window function.

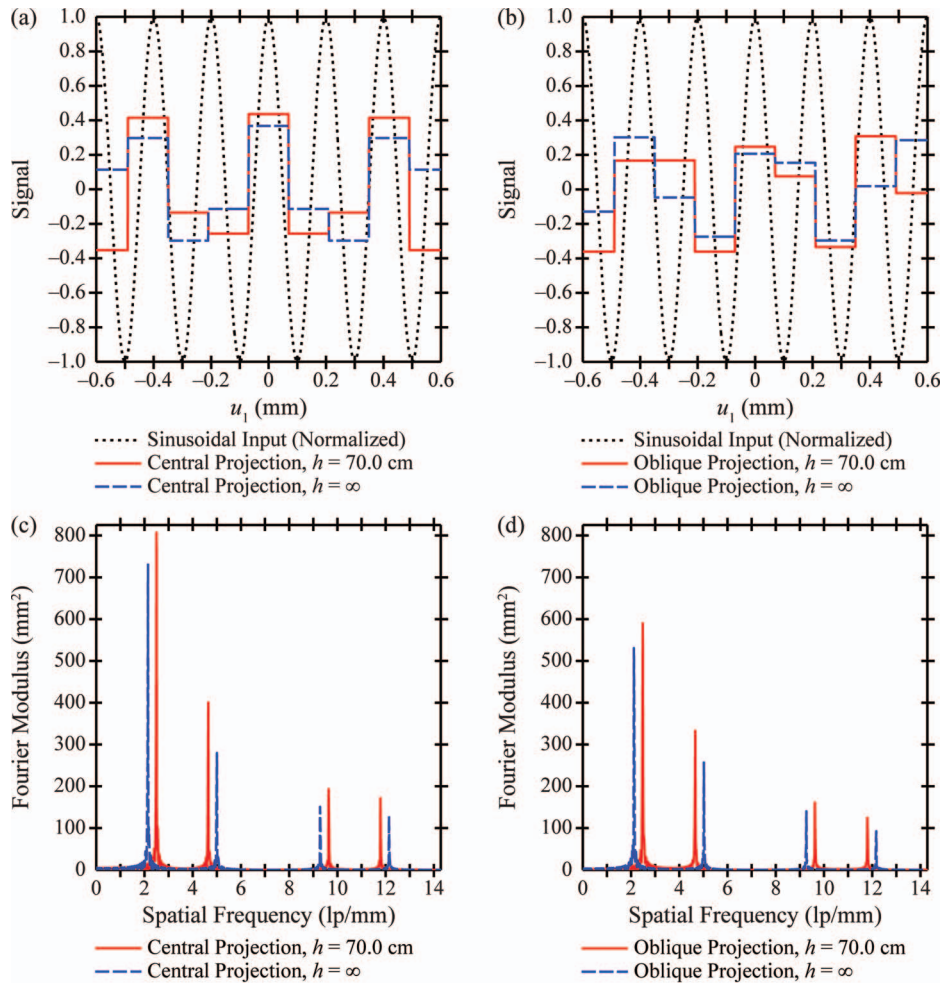


FIG. 4. At a distance u_2 of 30.0 mm from the chest wall, cross sections of detector signal in the central projection ($n = 0$) and the most oblique projection ($n = 7$) are plotted versus position u_1 . In addition, Fourier transforms are shown versus frequency. The major Fourier peaks do not occur at the input frequency 5.00 lp/mm, illustrating the presence of aliasing. Reducing the source-to-COR distance (h) magnifies the input frequency projected onto the detector.

position (u_1, u_2) by Eq. (15) but instead is always $\psi_n - \gamma_n$ for the n th projection.

In the parallel beam geometry, the central projection represents the input frequency as if it were $a^{-1} - f_0$, or $0.3a^{-1}$. As a result, the Fourier transform has a major peak at $0.3a^{-1}$ (2.14 lp/mm), and has minor peaks at $0.7a^{-1}$ (5.0 lp/mm), $1.3a^{-1}$ (9.29 lp/mm), and $1.7a^{-1}$ (12.14 lp/mm). Unlike the parallel beam geometry, the divergent beam geometry magnifies the input so that it projects onto the x-ray converter with the frequency f_0/M

$$M = \frac{h}{h - z_0}, \quad (88)$$

where M denotes the magnification.²¹ With a source-to-COR distance (h) of 70.0 cm and an object-to-detector distance (z_0) of 50.0 mm, M is 1.077. As a result of the magnification, the peaks in the Fourier transform of detector signal occur at different frequencies than the parallel beam geometry. Accordingly, these Fourier peaks occur at $a^{-1} - f_0/M$ (2.50 lp/mm), f_0/M (4.64 lp/mm), $2a^{-1} - f_0/M$ (9.64 lp/mm), and $a^{-1} + f_0/M$ (11.78 lp/mm). The Fourier transform of the

most oblique projection peaks at similar frequencies as the central projection.

III.A.2. SBP reconstruction

Figure 5(a) shows SBP reconstruction versus position (x) measured parallel to the chest wall side of the breast support, performed at the distance $y = 30.0$ mm from the chest wall and at the height $z = z_0 = 50.0$ mm above the detector. Unlike an individual projection, SBP reconstruction can resolve the input frequency 5.00 lp/mm. This property arises because the oblique projections give information about the input which is not present in the central projection alone [Fig. 4(b)]. Although not explicitly plotted in Fig. 5(a), it can be shown that super-resolution is present across a broad range of x and y positions in the reconstructed volume.

The SBP Fourier transform [Eq. (86)] correctly possesses its major peak at 5.00 lp/mm. The major peak of an individual projection, occurring at 2.50 lp/mm, is now highly suppressed in magnitude [Fig. 5(c)].

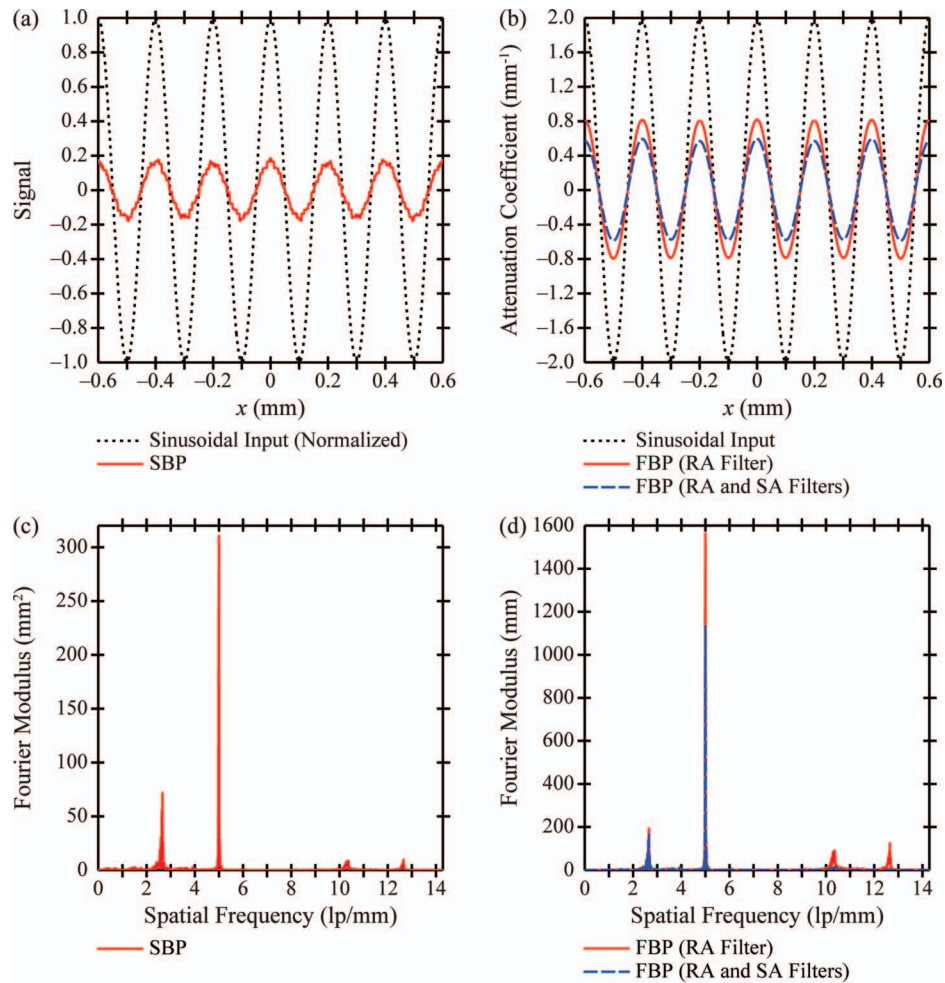


FIG. 5. Unlike a single projection (Fig. 4), simple backprojection (SBP) reconstruction can resolve a high frequency input oriented along the x direction. Applying filters to the reconstruction smoothens pixelation artifacts in the spatial domain and reduces low frequency spectral leakage in the Fourier domain. Reconstructing with the ramp (RA) filter alone has the benefit of greater modulation than reconstructing with the RA and spectrum apodization (SA) filters together. The drawback of reconstructing with the RA filter alone is increasing the amplitude of high frequency spectral leakage.

III.A.3. FBP reconstruction

FBP reconstructions are now performed with either the RA filter alone or the RA and SA filters together. In the spatial domain, these reconstructions are plotted versus position (x) parallel to the chest wall side of the breast support, assuming $y = 30.0$ mm and $z = 50.0$ mm [Fig. 5(b)]. Figure 5(b) demonstrates that reconstruction filters smoothens pixelation artifacts found in the SBP reconstruction. In addition, Fig. 5(b) shows that reconstructing with the RA filter alone yields greater modulation than reconstructing with the RA and SA filters together. The modulation for reconstruction with the RA filter alone is 41.0%, yet the modulation for reconstruction with the RA and SA filters together is 29.8%. It is expected that reconstruction with the RA filter alone has greater modulation, since the amplitude of this filter exceeds that of the RA and SA filters together at the input frequency (Fig. 3). Importantly, the modulation of either FBP reconstruction technique is well above the limit of resolution for typical imaging systems, which is often taken to be 5%. In addition, the modulation of either FBP reconstruction technique is greater than that of SBP reconstruction (18.4%).

Although reconstruction with the RA filter alone has the benefit of greater modulation than reconstruction with the RA and SA filters together, the tradeoff is greater spectral leakage at very high frequencies. In fact, the amplitude of the high frequency spectral leakage is greater with the RA filter alone than with SBP. In experimental practice, reconstruction with the RA filter alone also increases the presence of noise, which tends to occur at high frequencies.

III.B. Input frequency directed perpendicular to the chest wall

It is now demonstrated that the existence of super-resolution is dependent on the directionality of the input frequency. Super-resolution arises because of subpixel detector element shifts in the image of an object with each increasing projection angle. In order to investigate the feasibility of super-resolution for frequencies oriented along the y direction (i.e., perpendicular to the chest wall), the translational shift in the u_2 position of the incident x-ray is now calculated. For the n th projection, an x-ray passing from the focal

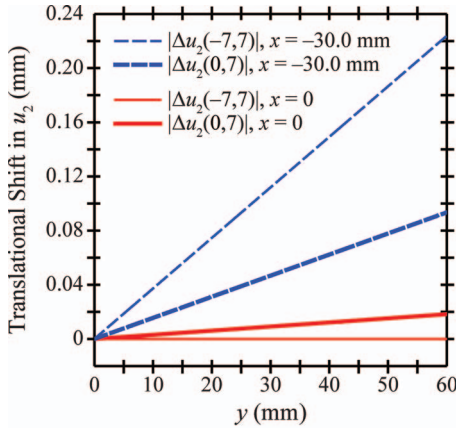


FIG. 6. At a reconstruction depth (z) of 50.0 mm, the magnitude of the translational shift in the u_2 coordinate of the image [Eq. (90)] is plotted versus position y measured perpendicular to the chest wall. In the mid PA/SS plane ($x = 0$), translational shifts are minimal comparing the central projection and an oblique projection ($n_1 = 0, n_2 = 7$), and are zero comparing the two most oblique projections ($n_1 = -7, n_2 = 7$). Increasing the magnitude of the distance x relative to the mid PA/SS plane yields a noticeable change in the translational shift.

spot through the point (x, y, z) strikes the detector at the u_2 coordinate

$$u_2(n) = \frac{y [l \cos \gamma_n + h \cos(\psi_n - \gamma_n)]}{x \sin \gamma_n + (l - z) \cos \gamma_n + h \cos(\psi_n - \gamma_n)}. \quad (89)$$

This expression follows from Eq. (16). The translational shift in the u_2 position of the object comparing projection numbers n_1 and n_2 is thus

$$\Delta u_2(n_1, n_2) = u_2(n_2) - u_2(n_1). \quad (90)$$

Assuming that $z = 50.0$ mm, Fig. 6 shows the magnitude of this translational shift versus position y within two planes, $x = 0$ and $x = -30.0$ mm, comparing the central projection and an oblique projection ($n_1 = 0, n_2 = 7$) as well as two oblique projections ($n_1 = -7, n_2 = 7$). Throughout the remainder of this work, a plane defined by a fixed value of x will be termed a PA/SS plane since it has extent in both the posteroanterior (PA) and source-to-support (SS) directions. Although the SS direction technically varies with position on the breast support due to the divergence of the x-ray beam, it is assumed to be equivalent to the z direction for the purpose of this work. As such, the SS direction lies along the same axis as the source-to-image distance (SID), or the length between the focal spot and the origin O for the central projection (Fig. 1). In a cranial-caudal (CC) view, a PA/SS plane is thus a sagittal plane through the breast. By contrast, in a medio-lateral oblique (MLO) view, the same plane is at an approximately 45° angle relative to the sagittal and transverse planes through the breast.

In the mid PA/SS plane ($x = 0$), translational shifts between projections are minimal in a typical sized breast. For example, with $x = 0, y = 30.0$ mm, and $z = 50.0$ mm, the translational shift between the central projection and an oblique projection is 0.009 mm (6.52% of detector element length), and the translational shift between the two most

oblique projections is zero. For this reason, super-resolution along the y direction is simply not achievable within the mid PA/SS plane. As illustrated in Fig. 7(a), SBP reconstruction at $x = 0$ in the region $y \in [29.4 \text{ mm}, 30.6 \text{ mm}]$ resembles a single projection.

In Fig. 6, it is demonstrated that the u_2 translational shift between projections increases as the magnitude of the distance x increases. For example, with $x = -30.0$ mm and $y = 30.0$ mm, the translational shift between the central projection and the oblique projection is 0.047 mm (33.4% of detector element length), and the translational shift between the two most oblique projections is 0.112 mm (80.0% of detector element length). Because these translational shifts are sufficiently large, SBP reconstruction [Fig. 7(c)] shows super-resolution at $x = -30.0$ mm over the region $y \in [29.4 \text{ mm}, 30.6 \text{ mm}]$. Unlike SBP reconstruction for an input frequency oriented along the x direction [Fig. 5(a)], the amplitudes of the peaks in Fig. 7(c) are noticeably different from each other, indicating the presence of reconstruction artifacts. It can be shown that these artifacts are minimized by increasing the distance y from the chest wall, since the u_2 translational shifts between projections increase with y (Fig. 6).

The SBP reconstructions in Fig. 7 can be analyzed further by computing their 1D Fourier transform along the y direction. To show differences in these Fourier transforms at fixed values of x , we choose not to transform over both x and y as given by Eq. (85)

$$\begin{aligned} \mathcal{F}_1 [\mathcal{B}(\mathcal{X}\mu)](x, f_y, z) &= \sum_{\mathbf{m}, n} \frac{D\mu(\mathbf{m}, n)}{N} \frac{e^{\frac{2\pi i f_y (\sigma_{3m} x + \sigma_{5m} z)}{\sigma_{4m}}} }{\sigma_{4m}} \\ &\cdot \text{rect} \left[\frac{(\sigma_{1m} x + \sigma_{2m} z) \sec \theta_{m} - m_x a_x}{a_x} \right] \mathcal{F}_1 \rho_2 \left(\frac{f_y}{\sigma_{4m}} \right). \end{aligned} \quad (91)$$

For additional proof that super-resolution is not achievable within the mid PA/SS plane, Fig. 7(b) shows that the major Fourier peak at $x = 0$ occurs well below the input frequency. By contrast, the major Fourier peak at $x = -30.0$ mm [Fig. 7(d)] matches the input frequency, 5.00 lp/mm. Although not shown in the plot, it can be demonstrated that spectral leakage is reduced by increasing the magnitude of the distance x relative to the mid PA/SS plane.

As a final point in this section, it is important to note that by applying the filters in Fig. 3 to the SBP reconstructions of Fig. 7, the modulation effectively vanishes (graph not shown). This finding arises because filtering is applied only within the plane of the chest wall [Eq. (40)]. An input frequency oriented along the y direction contributes a component of 0 lp/mm within the plane of the chest wall; since the reconstruction filters vanish at 0 lp/mm (Fig. 3), FBP reconstructions are expected to have no modulation. For this reason, future research on filter optimization is merited as described in the Discussion section.

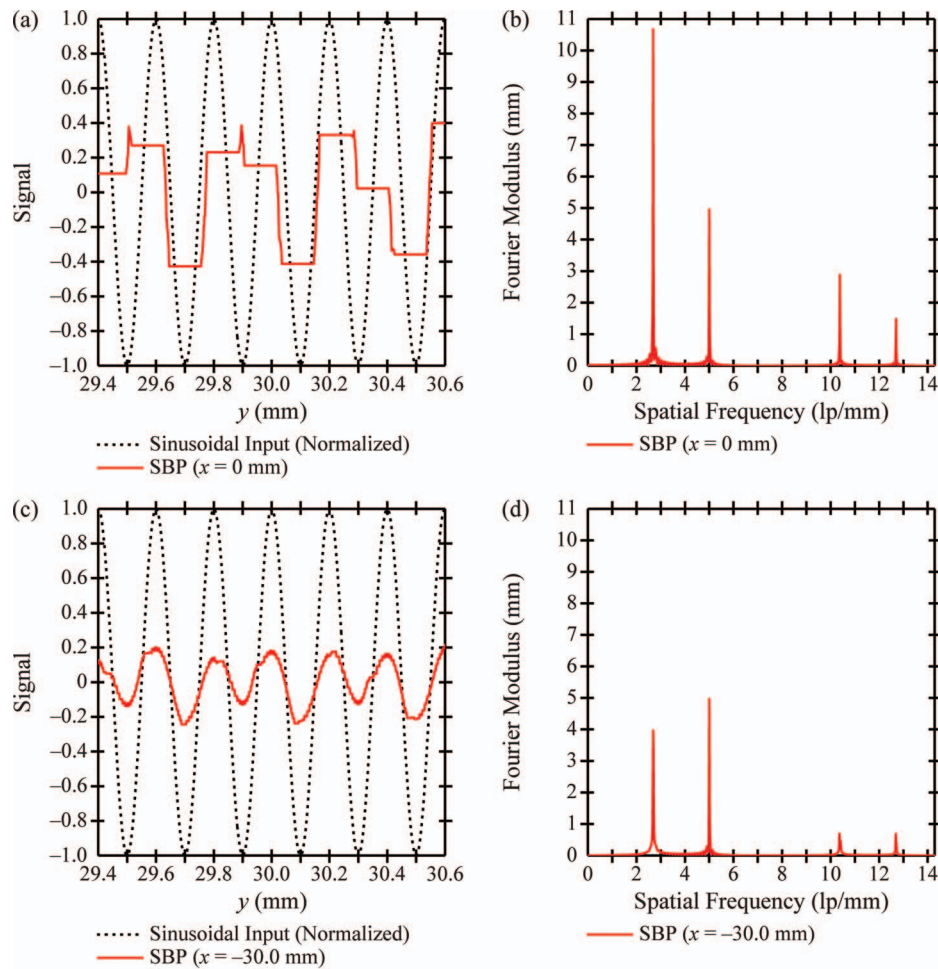


FIG. 7. (a) Within the mid PA/SS plane ($x = 0$), SBP reconstruction resembles a single projection over the region $y \in [29.4 \text{ mm}, 30.6 \text{ mm}]$ for an input frequency oriented along the y direction perpendicular to the chest wall. (b) The 1D Fourier transform of the SBP reconstruction is plotted versus frequency measured along the y direction. Within the mid PA/SS plane of a typical sized breast, the major Fourier peak occurs at a frequency lower than the input frequency, 5.00 lp/mm. (c) With $x = -30.0 \text{ mm}$, super-resolution in a SBP reconstruction is indeed achievable over the region $y \in [29.4 \text{ mm}, 30.6 \text{ mm}]$. (d) For additional proof of super-resolution at $x = -30.0 \text{ mm}$, the major peak of the corresponding Fourier transform occurs at the input frequency, 5.00 lp/mm.

III.C. Dependency of super-resolution on reconstruction depth

Using the Fourier transforms calculated in Secs. III.A and III.B, one can introduce a metric for assessing the quality of super-resolution in the reconstruction. This metric is the ratio (r) of the amplitude at the highest Fourier peak less than the detector alias frequency (3.57 lp/mm) to the amplitude at the input frequency (5.00 lp/mm). Super-resolution is present if $r < 1$ and is absent if $r \geq 1$. For high quality super-resolution, r should be as close to zero as possible.

To investigate anisotropies in super-resolution along the z direction, r is plotted versus the reconstruction depth (z_0) in Fig. 8(a), assuming an input frequency oriented along the x direction (Sec. III.A). In the Fourier transforms used for calculating r [Eq. (86)], the detector field-of-view (FOV) is 56.1 mm \times 84.1 mm, and is centered on the plane $x = 0$. Detector element indices m_x and m_y thus range from -200 to 200 and 0 to 600 , respectively. By centering the FOV on the region $x = 0$, anisotropies in super-resolution can be assessed within the mid PA/SS plane. Super-resolution is

not achievable at depths with sharp peaks in the value of r , including $z_0 = 28.7, 35.6, 42.2, 48.8, 55.2, 61.5, 67.6,$ and 73.7 mm . The depths considered in the plot span a typical 50.0 mm breast thickness. Because the width of each peak in Fig. 8(a) is very narrow, super-resolution is present at most depths in the reconstruction. Although only SBP is simulated, similar anisotropies arise if filters are used.

To illustrate the anisotropy of super-resolution along the z direction, Fig. 8(b) shows a SBP reconstruction at a depth ($z_0 = 42.2 \text{ mm}$) matching one of the peaks in Fig. 8(a). The reconstruction is performed at the distance $y = 30.0 \text{ mm}$ from the chest wall and over a region centered on the mid PA/SS plane (i.e., $x \in [-0.6 \text{ mm}, 0.6 \text{ mm}]$). Signal varies with position in a step-like manner analogous to an individual projection [Figs. 4(a) and 4(b)]. Consequently, super-resolution is not achievable at this depth, position, and orientation within the mid PA/SS plane.

A necessary condition for super-resolution is the presence of translational shifts in the image of an object between projections. This condition is not sufficient for super-resolution;

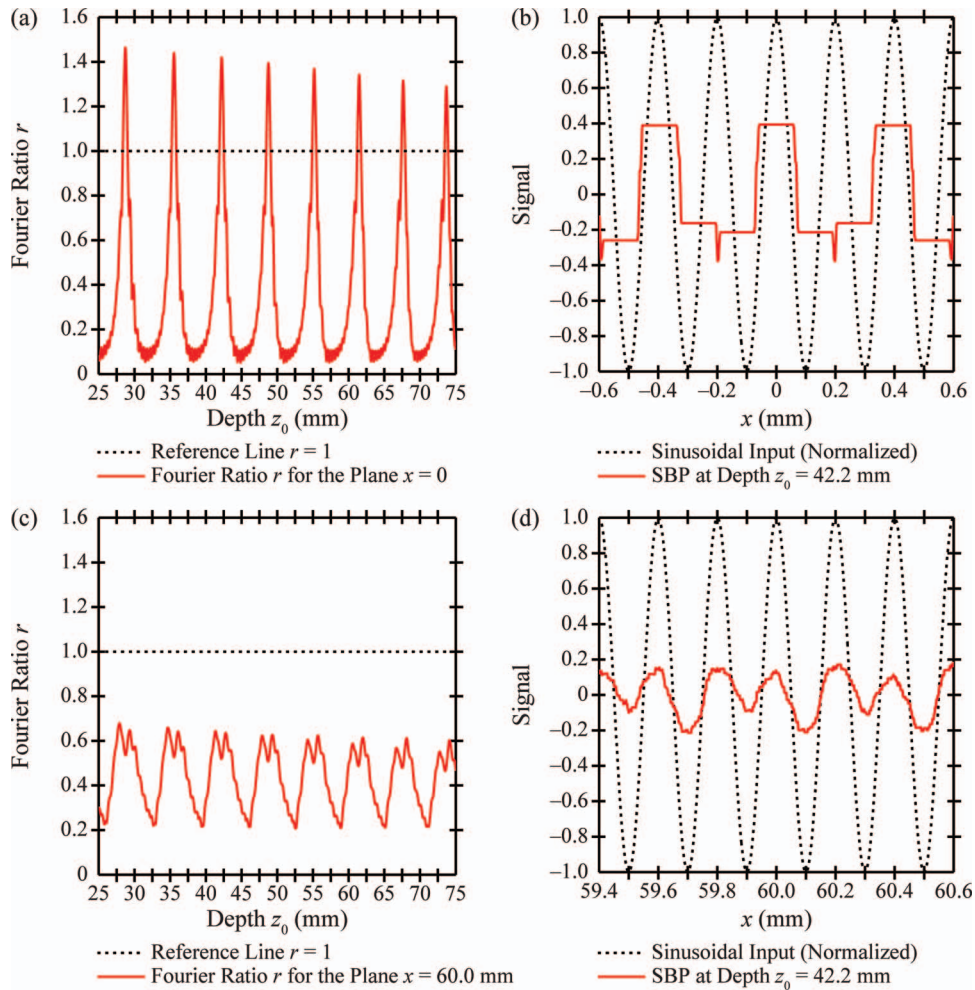


FIG. 8. For an input frequency oriented along the x direction, the dependency of super-resolution on depth (z_0) is analyzed. The existence of super-resolution is determined from the ratio (r) of the amplitude at the highest peak in the Fourier transform less than the alias frequency of the detector (3.57 lp/mm) to the amplitude at the input frequency (5.00 lp/mm). Super-resolution is present if $r < 1$ and is absent if $r \geq 1$. (a) and (b) Within the mid PA/SS plane ($x = 0$), super-resolution is not achievable at depths with sharp peaks in the value of r , such as $z_0 = 42.2$ mm. (c) and (d) By contrast, within the plane $x = 60.0$ mm, super-resolution is feasible at all depths; r never exceeds unity.

the translational shifts must be in increments that maximize subpixel sampling gain. If the image of a thin input object is translated between projections in increments that are approximately integer multiples of detector element length, the signal is effectively equivalent in all projections, and super-resolution cannot be achieved. For this reason, anisotropies in super-resolution occur at depths where translational shifts between projections have effectively no subpixel sampling differences.

Figure 8(c) investigates whether the depth-dependency of super-resolution also exists at positions that are displaced from the mid PA/SS plane ($x = 0$). Similar to Fig. 8(a), r is plotted versus depth (z_0); however, in the Fourier transforms used for calculating r [Eq. (86)], the detector FOV (56.1 mm \times 84.1 mm) is now centered on the plane $x = 60.0$ mm. Detector element indices m_x and m_y thus range from 229 to 629 and 0 to 600, respectively. In Fig. 8(c), r never exceeds unity, indicating that super-resolution is feasible at all depths within the plane

$x = 60.0$ mm. As a result, although Fig. 8(b) shows that super-resolution is not achievable at the depth $z_0 = 42.2$ mm within the plane $x = 0$, Fig. 8(d) demonstrates that super-resolution is indeed feasible at the same depth within the plane $x = 60.0$ mm. The value of r at the depth $z_0 = 42.2$ mm drops from 1.42 to 0.520 in shifting the central axis of the detector FOV from $x = 0$ to $x = 60.0$ mm.

Although Figs. 8(b) and 8(d) are plotted for a fixed value of y (30.0 mm), it can be shown that similar plots hold for all values of y . To explain this finding, it is useful to calculate the translational shift in the object position between projections along the u_1 direction; this direction is chosen because of the orientation of the input frequency in Secs. III.A and III.C

$$\Delta u_1(n_1, n_2) = u_1(n_2) - u_1(n_1), \quad (92)$$

where

$$u_1(n) = \frac{x(l + h \cos \psi_n) + zh \sin \psi_n}{x \sin \gamma_n + (l - z) \cos \gamma_n + h \cos(\psi_n - \gamma_n)}. \quad (93)$$

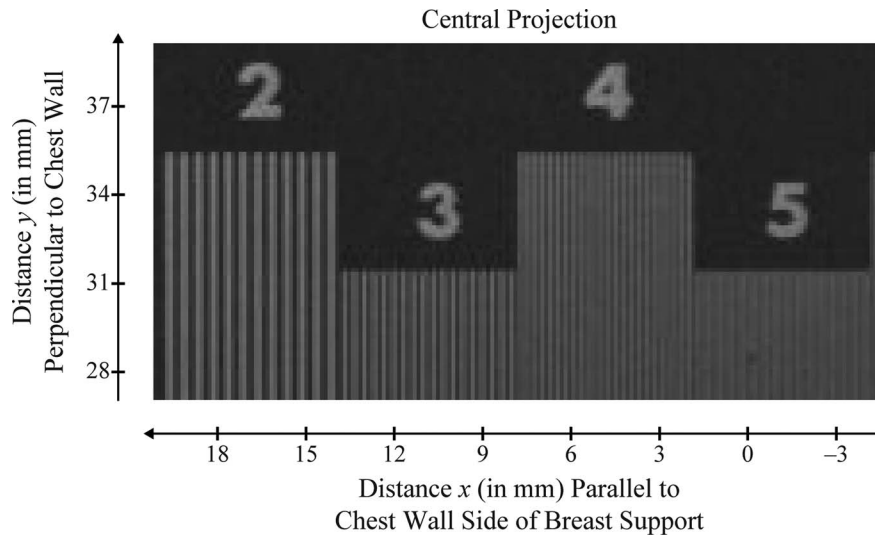


FIG. 9. The central projection of a bar pattern phantom misrepresents frequencies higher than the detector alias frequency, 3.57 lp/mm for 140 μm detector elements. For example, at 4.0 lp/mm, Moiré patterns are present. At 5.0 lp/mm, fewer than 30 line pairs are observed over a 6.0 mm length.

There is no y dependency in the formula for the translational shift. Consequently, for an input frequency oriented along the x direction, the existence of super-resolution is dependent only on the x and z coordinates in the reconstruction.

IV. EXPERIMENTAL RESULTS

Using a high contrast bar pattern phantom, we have experimentally verified the existence of super-resolution in DBT. The phantom was taped beneath the compression paddle (24 cm \times 29 cm) of the Selenia Dimensions system, and placed 2.5 cm above the breast support. With the alternating light and dark bands of the phantom spanning a 6.0 mm length, the line pairs ranged in frequency from 1.0 lp/mm to 10.0 lp/mm. To match the simulation of Sec. III.A, the frequency 5.0 lp/mm was oriented along the x direction parallel to the chest wall side of the breast support. Also, following the simulation, the bar patterns at 5.0 lp/mm covered the region $x \in [-0.6 \text{ mm}, 0.6 \text{ mm}]$, and the edge of the bar patterns near the numeral “5” (Fig. 9) was positioned slightly greater than $y = 30 \text{ mm}$ from the chest wall. Using the large (0.3 mm nominal) focal spot and a CC view, 15 projections were acquired at 30 kVp and 14 mAs with a W/AI target-filter combination. The technique for determining the optimal mAs with phototiming is described in our previous work.⁵

Reconstruction was subsequently performed using a back-projection filtering (BPF) commercial prototype reconstruction solution (BrionaTM, Real Time Tomography, Villanova, PA).²² Although it is possible to reconstruct on a non-pixelated grid using analytical modeling, a pixelated grid was required for the experimental data. In order to ensure that high frequencies can be resolved in the plane of the reconstruction, the pixel size of the reconstruction grid (20.44 μm) was chosen to be significantly smaller than that of the detector elements (140 μm). Consequently, the alias frequency of the reconstruction grid (24.46 lp/mm) was substantially higher than the alias frequency of the detector (3.57 lp/mm).

Figure 9 shows that the central projection correctly resolves frequencies below the detector alias frequency, 3.57 lp/mm. At the next highest frequency (4.0 lp/mm), one would expect to see 24 line pairs spanning a 6.0 mm length. Instead, less than 24 line pairs are visible, and Moiré patterns²³ are present. Finally, at 5.0 lp/mm, only 16 line pairs are evident within a 6.0 mm length, indicating that the pattern is incorrectly represented as a frequency between 2.0 and 3.0 lp/mm.

Unlike the central projection, BPF reconstruction can resolve frequencies higher than the detector alias frequency (Fig. 10). In fact, up to 6.0 lp/mm (36 line pairs spanning 6.0 mm) can be observed at the correct orientation with no Moiré patterns. At 7.0 lp/mm, the signal becomes too faint to distinguish bar patterns. This finding arises because the MTF of the reconstruction is reduced with increasing frequency; recall from Eq. (87) that the MTF of the detector sampling process vanishes at the frequency $f_1 = a^{-1}$ (7.14 lp/mm), assuming $f_2 = 0$. As expected from the analytical modeling, it should be noted that super-resolution along the x direction was observed over many different x-ray acquisitions in which the bar pattern phantom was placed at various positions in the imaging volume.

By rotating the bar pattern phantom 90°, the potential for super-resolution orthogonal to the chest wall was also analyzed (Fig. 11). To orient the reader with the positioning of the phantom, it is important to note that the left edges of the even numerals “4” and “6” were aligned on the mid PA/SS plane ($x = 0$), and that the separation between 4.0 and 5.0 lp/mm was positioned at a displacement $y = 30 \text{ mm}$ from the chest wall. As expected from the analytical modeling (Sec. III.B), the extreme left regions of the bar patterns show aliasing of high frequencies due to their proximity to the mid PA/SS plane. Super-resolution is only present at the extreme right of the bar patterns (5.0 and 6.0 lp/mm), where the magnitude of the distance x relative to the mid PA/SS plane is approximately 30 mm or greater.

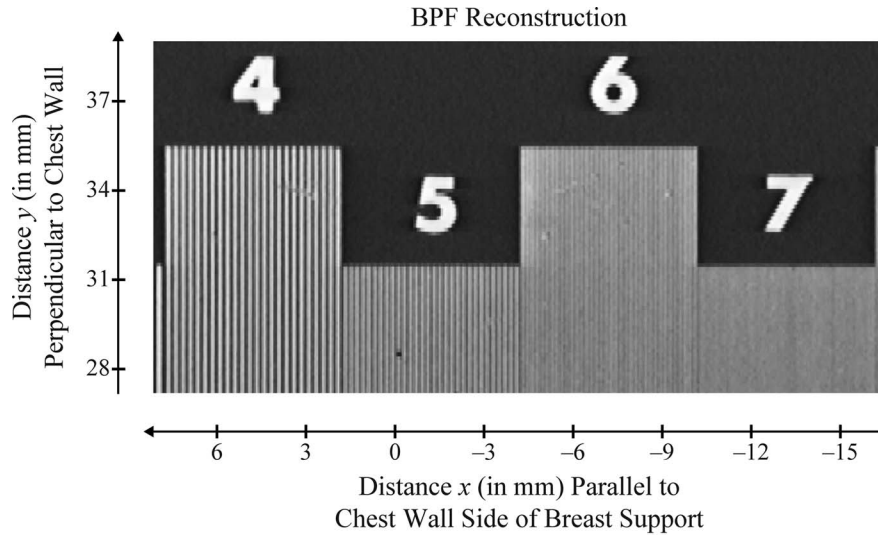


FIG. 10. Unlike the central projection (Fig. 9), BPF reconstruction can clearly resolve high frequencies along the x direction parallel to the chest wall side of the breast support. Frequencies up to 6.0 lp/mm are resolved with no Moiré patterns or other evidence of aliasing.

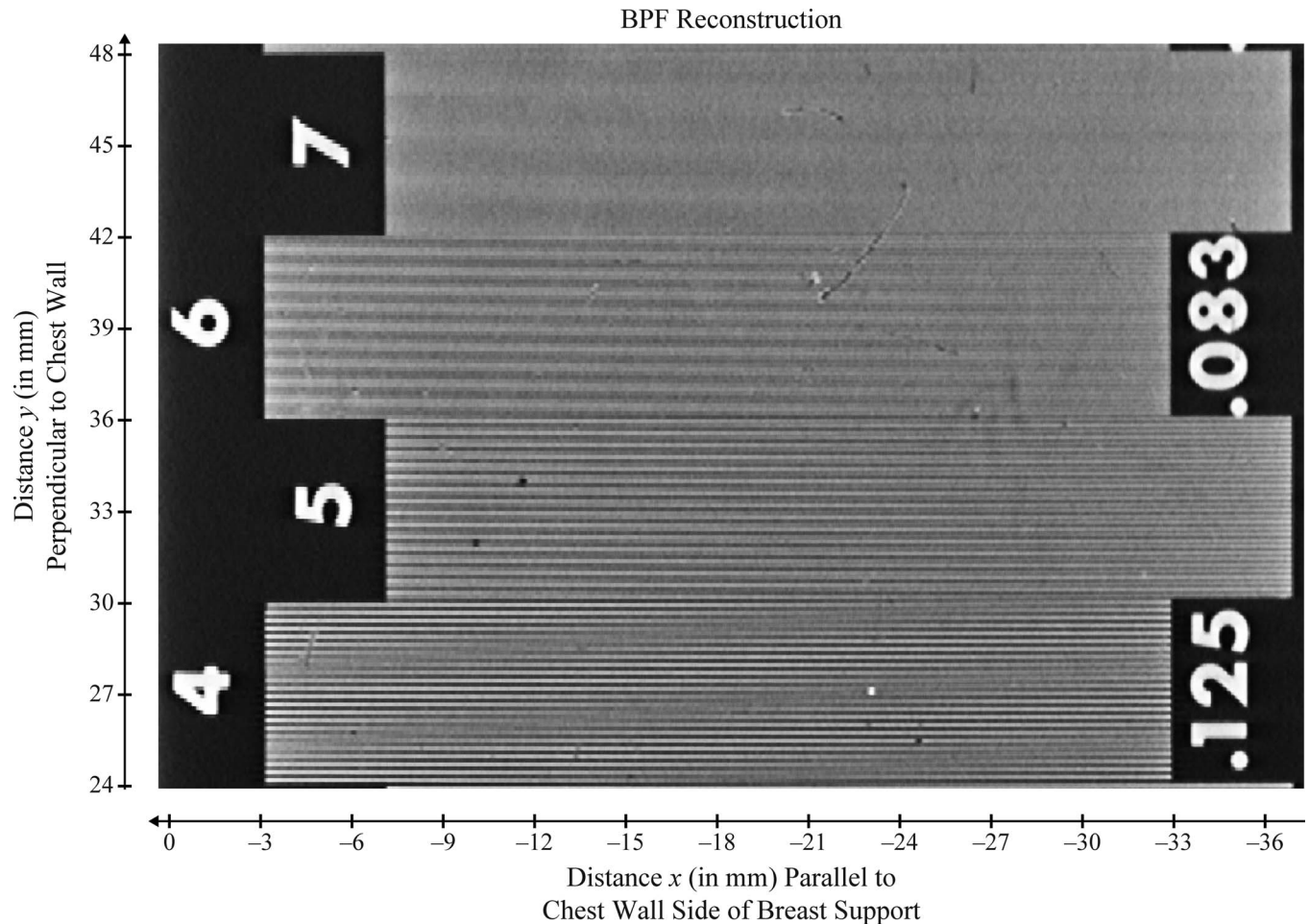


FIG. 11. Super-resolution along the y direction is analyzed with bar patterns using a BPF reconstruction. The left edges of the even numerals (“4” and “6”) were aligned on the mid PA/SS plane ($x = 0$), and the separation between 4.0 and 5.0 lp/mm was positioned 30 mm from the chest wall. At the extreme left of the bar patterns, less line pairs are visible than expected, illustrating that super-resolution is not achievable near the plane $x = 0$. In addition, Moiré patterns at 4.0 lp/mm indicate that super-resolution is not possible too close to the chest wall ($y = 0$). Super-resolution is evident only at positions sufficiently displaced from the planes $x = 0$ and $y = 0$; see the extreme right of the bar patterns at 5.0 and 6.0 lp/mm.

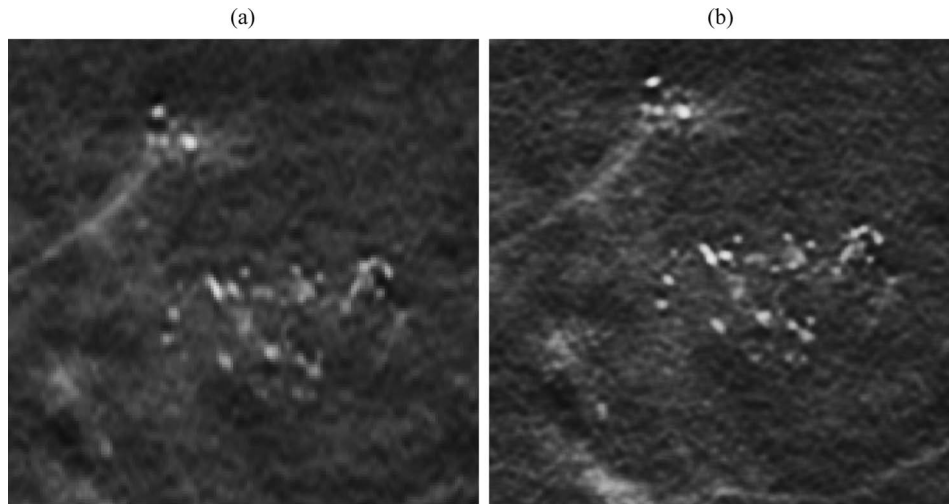


FIG. 12. Clinical images of microcalcifications are shown. In (a), BPF reconstruction is performed with pixels matching the detector element size ($140\ \mu\text{m}$), and the result is magnified fourfold to give the image that is shown. In (b), BPF reconstruction is performed using pixels that are much smaller than the detector elements. Image (b) supports super-resolution.

It is important to note that the extreme right of the bar patterns at $4.0\ \text{lp/mm}$ does not display super-resolution as cleanly as the extreme right of the bar patterns at 5.0 and $6.0\ \text{lp/mm}$ due to the presence of Moiré patterns. Recall that the phantom is positioned so that lower frequencies are closer to the chest wall. Because the u_2 translational shift between projections is minimized with decreasing distance from the chest wall (Fig. 6), it is expected that super-resolution along the y direction should not be achievable at positions too close to the chest wall.

In clinical images, super-resolution should improve the visibility of fine structural details in the breast. This concept is illustrated in Fig. 12 showing microcalcifications, which are early indicators of breast cancer in many women.²⁴ In the figure, the left image [Fig. 12(a)] is created by magnifying a BPF reconstruction performed with pixels matching the size of the detector elements ($140\ \mu\text{m}$). The final result has $35\ \mu\text{m}$ pixels (i.e., a fourfold magnification). By contrast, the right image [Fig. 12(b)] is generated by performing a BPF reconstruction using pixels that are much smaller than the detector elements. As expected from our analysis of bar patterns, the image is sharper in Fig. 12(b) than in Fig. 12(a), since Fig. 12(b) is capable of resolving high frequency information exceeding the detector alias frequency. Quantifying the clinical impact of this finding is beyond the scope of this work.

V. DISCUSSION

In DBT reconstructions using grids with the same pixel size as the detector elements, the highest frequency that can be resolved in each reconstructed slice is the detector alias frequency. This study demonstrates that reconstruction grids with much smaller pixelation display super-resolution, or visibility of higher frequencies. Super-resolution arises because the image of the object is shifted in subpixel detector element increments with each increasing projection angle.

Super-resolution was first demonstrated analytically by calculating the reconstruction of a sinusoidal input whose frequency was oriented along the x direction parallel to the chest wall side of the breast support. Using an infinitesimally fine reconstruction grid, it was shown that both SBP and FBP can resolve higher frequencies than a single projection. FBP reconstructions were performed either with the RA filter alone or with the RA and SA filters together. Although reconstruction with the RA filter alone has the benefit of greater modulation in the spatial domain, it presents the tradeoff of increased noise and spectral leakage at high frequencies.

In rotating the sine plate by 90° , super-resolution was found to exist at fewer positions in the reconstruction. For an input frequency oriented along the chest wall-to-nipple direction, it was shown that positions with super-resolution must be displaced relative to the chest wall ($y = 0$) and to the mid PA/SS plane ($x = 0$). At these positions, the translational shifts in the image between projections are sufficiently large to achieve super-resolution. Because increasing the angular range of the scan inherently increases the translational shifts between projections, the exact positions at which super-resolution is feasible are dependent upon the design of the acquisition geometry.

This paper also demonstrates that the existence of super-resolution is depth-dependent. Considering an input frequency oriented along the x direction for illustration, it was shown that super-resolution is not feasible at certain depths (z) within the mid PA/SS plane. By contrast, super-resolution is achievable at all depths within PA/SS planes that are sufficiently displaced relative to the mid PA/SS plane. The anisotropies in super-resolution along the z direction are dependent upon the number of projections and the angular spacing between projections.

We have experimentally observed super-resolution in images of bar patterns. A single projection showed classical signs of aliasing, including Moiré patterns and the visibility of fewer line pairs than expected. By contrast, reconstructions

using very fine grids resolved frequencies higher than the alias frequency of the detector. For the two orientations of the bar patterns, the presence of super-resolution was verified at positions predicted from analytical modeling. The effects observed in the experimental images are not necessarily unique attributes of the commercial DBT system or the commercial reconstruction algorithm used. Super-resolution should be feasible provided the detector has measurable modulation above the alias frequency and the reconstruction algorithm supports finer sampling than the detector in each reconstructed slice.

Super-resolution appears to produce a sharper image of microcalcifications showing more detail. This finding is complementary to prior work on computer breast phantoms demonstrating that fiducial markers can be located with higher precision in a supersampled reconstruction.²⁵ It is important to determine the effect of super-resolution on noise, and to evaluate the potential benefits of super-resolution using a task-based approach. A future clinical study is also merited to assess the clinical impact of super-resolution in DBT.

Super-resolution is a particularly useful property for x-ray systems that employ binning when switching from 2D to 3D imaging modes. For example, in the Selenia Dimensions system, the DM detector element dimensions are $70\ \mu\text{m} \times 70\ \mu\text{m}$, whereas the DBT detector element dimensions are $140\ \mu\text{m} \times 140\ \mu\text{m}$. Binning has the benefit of lowering the readout time, but presents the drawback of reducing the alias frequency of the detector. Initially, it would seem that binning should make DBT less capable of resolving high frequency information, such as microcalcifications. However, the existence of super-resolution in the reconstruction may counter the tradeoffs of binning.

Some of the limitations of this study and directions for future modeling are now noted. In calculating detector signal, this paper assumes that the MTF of *a*-Se in drift mode is unity. While this assumption is valid for normal x-ray incidence, it is less justifiable with oblique x-ray incidence.^{26–33} Que and Rowlands proposed the first analytical model of the optical transfer function (OTF) of *a*-Se in drift mode for all incident angles.²⁶ Their work was later validated by Hajdok and Cunningham with Monte Carlo simulations.²⁷ Denoting μ_{Se} as the attenuation coefficient of Se and L as the thickness of the photoconductor, the OTF at each frequency f is

$$\text{OTF}(f) = \frac{[1 - e^{-(\mu_{\text{Se}}L \sec \theta_n + 2\pi i f L \tan \theta_n)}] \cos \theta_n}{1 + \frac{2\pi i f \sin \theta_n}{\mu_{\text{Se}}}}. \quad (94)$$

The MTF is the normalized modulus of the OTF. For more thorough modeling, signal in the x-ray converter should be convolved with the point spread function (PSF) of *a*-Se before detector element sampling is performed, where the PSF is determined from the OTF using Fourier theory. It is important to model MTF degradation for measurements near the edge of the detector opposite the chest wall, as the incident angle deviates considerably from the normal. Upon examining θ_n across multiple projections in the Selenia Dimensions detector, it can be shown that the maximum incident angle is approximately 25° . Assuming $200\ \mu\text{m}$ thick *a*-Se and $20\ \text{keV}$

x-rays^{34–36} for which μ_{Se} is $20.5\ \text{mm}^{-1}$,³⁷ the corresponding MTF at $5.0\ \text{lp/mm}$ is 85.8% .

While it is important to consider MTF degradation at positions distal to the chest wall, it is less critical for positions close to the chest wall. For example, in the central projection at the position $u_1 = u_2 = 30.0\ \text{mm}$, the incident angle is 3.47° , and the MTF at $5.0\ \text{lp/mm}$ is 99.7% . Consequently, for the purpose of this work, an x-ray converter with MTF of unity was assumed.

In addition to modeling the MTF of the x-ray converter, the analytical model of the sine plate can be refined by modeling the MTF of the focal spot. Although this paper assumes a point-like focal spot that is stationary during each projection, future studies should model MTF degradation with increasing focal spot size³⁸ and increasing focal spot motion during a continuous scan of the projections.^{14,39,40} Our earlier work has shown that continuous x-ray tube motion yields a loss of modulation in the reconstruction.⁴¹ Despite this increase in blurring, super-resolution should still be achievable in the reconstruction of the sine plate (Figs. 5, 7, and 8). This claim is supported by the presence of super-resolution in bar pattern images (Figs. 10 and 11), which were acquired on a DBT system with continuous tube motion.

In future studies, detector lag and ghosting^{42–44} should also be simulated, and the presence of shot noise⁴⁵ should be modeled at various dose levels. Because this work considers a high contrast input frequency either with the analytical simulation or with the experimental bar patterns, it was not necessary to model the presence of noise at different dose levels. Future studies on super-resolution with low contrast input frequencies will require a noise simulation, as the visibility of the patterns should be influenced by dose. Finally, because the linear attenuation coefficient of an input object is energy dependent, polyenergetic x-ray spectra^{46–48} should also be simulated in the analytical model. This work implicitly assumes a monoenergetic x-ray beam.

In CT, the conventional low frequency filter is the RA filter^{14,15} which increases linearly with frequency from zero (Fig. 3). Assuming that filtering is only applied within the plane of the x-ray tube motion, this work demonstrates that the RA filter is not suited for imaging frequencies perpendicular to the chest wall, since the modulation of the reconstruction vanishes (Sec. III.B). The filters used in the experimental reconstructions of bar patterns oriented perpendicular to the chest wall (Fig. 11) have a nonzero offset at $0\ \text{lp/mm}$, unlike the RA filter used in the analytical modeling. Future work should consider filters with nonzero offset for analytical modeling of super-resolution, since modulation would not be zero for any orientation of the input frequency.

Because super-resolution has important clinical applications in improving the visibility of microcalcifications, future work should ultimately transition from modeling a sinusoidal input to simulating microcalcifications in a breast background.⁴⁹ Using model observers, improvements in the visibility of microcalcifications should be assessed with image reconstructions at varying grid sizes. It would be useful to determine the coarsest grid size at which the benefits of super-resolution are achieved among observers, as

reconstructions on coarser grids require less memory for data storage.

VI. CONCLUSION

This work demonstrates the existence of super-resolution in DBT. An analytical model of super-resolution was developed by calculating the reconstruction of a high frequency sinusoidal input. While a single projection cannot resolve frequencies higher than the alias frequency of the detector, a reconstruction on a very fine grid can resolve these frequencies. Super-resolution is made possible by the subpixel detector element shifts in the image of the object between projections.

Using a bar pattern phantom, we have experimentally verified the existence of super-resolution in DBT. In considering an input frequency that was oriented either parallel to the chest wall side of the breast support or perpendicular to the chest wall, the experimental images confirmed the presence of super-resolution at positions predicted by analytical modeling. Super-resolution has the potential to impact the visualization of microcalcifications and other subtle signs of breast cancer.

ACKNOWLEDGMENTS

The authors thank Baorui Ren (Hologic Inc., Bedford, MA) for providing useful background information on the acquisition geometry of the Selenia Dimensions tomosynthesis system. In addition, we gratefully acknowledge the assistance of Michael O'Shea and Roshan Karunamuni (University of Pennsylvania, Philadelphia, PA) in the acquisition of the bar pattern images showing the experimental feasibility of super-resolution in DBT. Also, we thank Johnny Kuo, Susan Ng, Peter Ringer (Real Time Tomography, LLC, Villanova, PA), and Predrag Bakic (University of Pennsylvania) for their help in reconstructing bar pattern and clinical images. Finally, we are grateful to David Pokrajac (Delaware State University, Dover, DE) for helpful feedback on improving the efficiency of MATLAB coding. Andrew D. A. Maidment is the chair of the Scientific Advisory Board of Real Time Tomography.

The project described was supported by Grant No. T32EB009384 from the National Institute of Biomedical Imaging and Bioengineering (NIBIB). The content is solely the responsibility of the authors and does not necessarily represent the official views of the NIBIB or the National Institutes of Health (NIH). Additional support for R.J.A. was provided by predoctoral training Grant No. W81XWH-11-1-0100 through the Department of Defense Breast Cancer Research Program. Support for Real Time Tomography was provided separately through NIH Grant No. R43EB007140/R44EB007140.

APPENDIX A: DETECTOR SIGNAL FOR AN INPUT FREQUENCY DIRECTED PERPENDICULAR TO THE CHEST WALL

This appendix calculates detector signal for an input frequency perpendicular to the chest wall. Under this assumption,

the input rectangular prism of thickness ε has a linear attenuation coefficient $\mu(x, y, z)$ which varies sinusoidally along the y direction with frequency f_0

$$\mu(x, y, z) = C \cdot \cos[2\pi f_0(y - y_0)] \cdot \text{rect}\left(\frac{z - z_0}{\varepsilon}\right), \quad [\text{cf. Eq. (1)}], \quad (\text{A1})$$

where y_0 is a translational shift in the waveform relative to the origin. The amplitude C of the waveform is equivalent to $1/\varepsilon$ upon normalizing total attenuation along the z direction. The 1D Fourier transform of Eq. (A1) along the y direction peaks at the frequencies $f_y = \pm f_0$ and vanishes at all other frequencies, following a formula similar to Eq. (4) with the exchange of x_0 for y_0 and f_x for f_y . Using Eqs. (17)–(19) and Eq. (22), total x-ray attenuation versus position (u_1, u_2) along the plane of the rotated detector is calculated for the n th projection as

$$\begin{aligned} \mathcal{A}\mu(n) &= \kappa_n \int_{w_n^+}^{w_n^-} \cos(2\pi f_0 u_2 w + \Lambda) dw, \quad [\text{cf. Eq. (23)}] \quad (\text{A2}) \\ &= \frac{\kappa_n (\sin[2\pi f_0 u_2 w_n^- + \Lambda] - \sin[2\pi f_0 u_2 w_n^+ + \Lambda])}{2\pi f_0 u_2}, \\ & \quad [\text{cf. Eq. (24)}] \quad (\text{A3}) \end{aligned}$$

where

$$\Lambda = -2\pi f_0 y_0, \quad [\text{cf. Eq. (26)}]. \quad (\text{A4})$$

Following the sum-to-product trigonometric identity given in Eq. (27), one may rewrite Eq. (A3) as

$$\begin{aligned} \mathcal{A}\mu(n) &= \kappa_n (w_n^- - w_n^+) \cos[\pi f_0 u_2 (w_n^+ + w_n^-) + \Lambda] \\ & \quad \cdot \text{sinc}[f_0 u_2 (w_n^- - w_n^+)], \quad [\text{cf. Eq. (28)}] \quad (\text{A5}) \\ &= \frac{\varepsilon \kappa_n \cos\left[\frac{2\pi f_0 u_2 (l+h \cos \psi_n - z_0)}{l+h \cos \psi_n - u_1 \sin \gamma_n} + \Lambda\right] \text{sinc}\left[\frac{\varepsilon f_0 u_2}{l+h \cos \psi_n - u_1 \sin \gamma_n}\right]}{l+h \cos \psi_n - u_1 \sin \gamma_n}, \\ & \quad [\text{cf. Eq. (29)}]. \quad (\text{A6}) \end{aligned}$$

The logarithmically transformed signal in the \mathbf{m} th detector element for the n th projection is now determined from Eq. (31). The midpoint formula⁵⁰ for approximating this double integral is

$$\begin{aligned} \mathcal{D}\mu(\mathbf{m}, n) &= \lim_{J_y \rightarrow \infty} \sum_{j_y=1}^{J_y} \frac{1}{J_y} \left[\lim_{J_x \rightarrow \infty} \sum_{j_x=1}^{J_x} \frac{\mathcal{A}\mu(j_x, j_y, n)}{J_x} \right], \\ & \quad [\text{cf. Eq. (35)}] \quad (\text{A7}) \end{aligned}$$

where

$$\begin{aligned} \mathcal{A}\mu(j_x, j_y, n) &\equiv \mathcal{A}\mu(n)|_{(u_1, u_2)} = \left(a_x \left[\frac{j_x - 1/2}{J_x} + m_x - \frac{1}{2} \right], a_y \left[\frac{j_y - 1/2}{J_y} + m_y \right] \right), \quad [\text{cf. Eq. (36)}]. \\ & \quad (\text{A8}) \end{aligned}$$

FBP reconstruction now follows from Eq. (42).

APPENDIX B: NOMENCLATURE

Symbol	Meaning		
•	Dot product operator.	CC	Cranial-caudal.
*	Convolution operator.	COR	Center-of-rotation of x-ray tube motion.
×	Cross product operator.	CT	Computed tomography.
∈	Set membership.	d_n	Distance between points G and O (Fig. 2).
$A\mu(n)$	Total attenuation for the n th projection.	DBT	Digital breast tomosynthesis.
$\tilde{A}\mu(n)$	A useful approximation for total attenuation [Eqs. (32) and (33)].	DM	Digital mammography.
\mathcal{B}	Backprojection operator.	f	Spatial frequency (f_0 denotes the input frequency).
$\mathcal{D}\mu(\mathbf{m}, n)$	Signal in the \mathbf{m} th detector element for the n th projection.	FBP	Filtered backprojection.
\mathcal{F}	Fourier transform operator (subscript denotes dimension).	FOV	Field-of-view.
\mathcal{L}_n	Path length through the input for the n th projection.	g	Gear ratio of detector.
\mathbb{R}^3	Euclidean three-space.	h	Source-to-COR distance for rotating x-ray tube.
$\mathcal{S}\mu(u_1, u_2)$	Raw signal at coordinate (u_1, u_2) on the rotated detector.	i	Imaginary unit given as $\sqrt{-1}$.
\mathcal{X}	X-ray transform operator.	I_{xmn}	An integral defined by Eq. (81).
\mathbb{Z}	Set of integers.	$I_{ymn}(x)$	An integral defined by Eq. (76).
\mathbb{Z}^*	Set of non-negative integers.	l	Distance between the COR and the midpoint of the chest wall side of the detector.
γ_n	Angle of rotation of the detector relative to the x axis for the n th projection.	L	Thickness of a -Se photoconductor in Eq. (94).
Γ_{mn}	Angle of backprojection within the plane of the detector [Eqs. (53) and (54)].	lp	Line pairs.
δ	Delta function.	\mathbf{m}	A doublet with coordinates (m_x, m_y) used for labeling detector elements.
$\Delta\psi$	Angular spacing between projections.	M	Magnification.
$\Delta u_j(n_1, n_2)$	Translational shift in u_j coordinate of incident ray comparing projection numbers n_1 and n_2 , where j varies between 1 and 2.	MLO	Mediolateral oblique.
ε	Thickness of sine plate (Fig. 1).	MRI	Magnetic resonance imaging.
θ_n	Angle of x-ray incidence relative to the normal to the detector (θ_{mn} denotes the special case at the centroid of the \mathbf{m} th detector element for the n th projection).	MTF	Modulation transfer function.
κ_n	A quantity defined by Eq. (25).	n	Projection number.
λ_n	A quantity defined by Eq. (26).	N	Total number of projections.
Λ	A quantity defined by Eq. (A4).	OTF	Optical transfer function.
μ	X-ray linear attenuation coefficient of input object (sine plate).	PA	Posteroanterior (in breast x-ray imaging, the direction perpendicular to the chest wall).
μ_{Se}	X-ray linear attenuation coefficient of a -Se photoconductor.	PA/SS	Descriptive acronym for a plane with extent along the posteroanterior (PA) and source-to-support (SS) directions.
ξ	Truncation frequency of reconstruction filter.	r	Ratio of the amplitude at the highest Fourier peak less than the detector alias frequency ($0.5a^{-1}$) to the amplitude at the input frequency (e.g., 5.00 lp/mm) in reconstructing a high frequency sine plate (Fig. 1).
ρ_1, ρ_2	Quantities defined by Eqs. (66) and (67).	RA	Ramp filter.
σ_{jmn}	Terms defined by Eqs. (68)–(72) used to simplify intermediate calculations, where j varies from 1 to 5.	SA	Spectrum apodization filter.
ϕ	Reconstruction filter.	SBP	Simple backprojection.
ψ_n	Nominal projection angle.	SID	Source-to-image distance (commonly measured between the focal spot and the midpoint of the chest wall side of the detector in the central projection).
a_x, a_y	Detector element dimensions in the x and y directions; if the x and y subscripts are removed, the detector element is square ($a_x = a_y = a$).	SNR	Signal-to-noise ratio.
b_1, b_2	Real numbers used to illustrate a sum-to-product trigonometric identity [Eq. (27)].	SS	Source-to-support (defined to be synonymous with the z direction).
BPF	Backprojection filtering.	t_1, t_2	Affine parameters of the x-ray transform.
C	Amplitude of attenuation coefficient of sine plate [Eq. (1)] taken to be $1/\varepsilon$.	TFT	Thin-film transistor.
		u_1, u_2	Position in the plane of the rotated detector (parallel and perpendicular to the chest wall, respectively).
		w	Parameter ranging between 0 and 1 in the equation of the x-ray beam between the focal spot and the incident point on the detector [Eq. (16)].

w_n^\pm	Value of w at the entrance (w_n^+) and exit (w_n^-) points of the x-ray beam through the sine plate (Fig. 1) for the n th projection.
x	Position parallel to the chest wall side of the breast support; rotation by the angle γ_n about the y axis yields x'_n .
x_0	Translational shift in the input waveform along the x direction [Eq. (1)].
y	Position perpendicular to the chest wall; it is equivalent to y'_n .
y_0	Translational shift in the input waveform along the y direction [Eq. (A1)].
z	Position relative to the origin O (Fig. 1) measured perpendicular to the plane of the breast support; rotation by the angle γ_n about the y axis yields z'_n .
z_0	Central height of the input object relative to the midpoint of the chest wall side of the detector.

^{a)} Author to whom correspondence should be addressed. Electronic mail: Andrew.Maidment@uphs.upenn.edu; Telephone: +1-215-746-8763; Fax: +1-215-746-8764.

¹ E. A. Rafferty, "Tomosynthesis: New weapon in breast cancer fight," *Decisions in Imaging Economics* **17**(4) (2004).

² S. P. Poplack, T. D. Tosteson, C. A. Kogel, and H. M. Nagy, "Digital breast tomosynthesis: Initial experience in 98 women with abnormal digital screening mammography," *Am. J. Roentgenol.* **189**(3), 616–623 (2007).

³ S. C. Park, M. K. Park, and M. G. Kang, "Super-resolution image reconstruction: A technical overview," *IEEE Signal Process. Mag.* **20**(3), 21–36 (2003).

⁴ J. T. Bushberg, J. A. Seibert, M. Edwin, J. Leidholdt, and J. M. Boone, "Image quality," in *The Essential Physics of Medical Imaging*, 2nd ed., edited by J.-R. John, A. Snyder, and T. DeGeorge (Lippincott, Philadelphia, PA, 2002), Chap. 10, pp. 255–291.

⁵ R. J. Acciavatti and A. D. A. Maidment, "Investigating the potential for super-resolution in digital breast tomosynthesis," in *SPIE Medical Imaging*, edited by N. J. Pelc, E. Samei, and R. M. Nishikawa (SPIE, Lake Buena Vista, FL, 2011), pp. 79615K-1–79615K-12.

⁶ H. H. Barrett and K. J. Myers, "Fourier analysis," in *Foundations of Image Science*, edited by B. E. A. Saleh (Wiley, New York, NY, 2004), Chap. 3, pp. 95–174.

⁷ D. L. Lee, L. K. Cheung, B. Rodricks, and G. F. Powell, "Improved imaging performance of a 14 × 17-inch direct radiography (TM) system using Se/TFT detector," in *SPIE Conference on Physics of Medical Imaging*, edited by T. James, I. Dobbins, and J. M. Boone (SPIE, San Diego, CA 1998), pp. 14–23.

⁸ T. Jing *et al.*, "Amorphous silicon pixel layers with cesium iodide converters for medical radiography," *IEEE Trans. Nucl. Sci.* **41**(4), 903–909 (1994).

⁹ A. R. Cowen, S. M. Kengyelics, and A. G. Davies, "Solid-state, flat-panel, digital radiography detectors and their physical imaging characteristics," *Clin. Radiol.* **63**, 487–498 (2008).

¹⁰ V. V. Nagarkar, T. K. Gupta, S. R. Miller, Y. Klugerman, M. R. Squillante, and G. Entine, "Structured CsI(Tl) scintillators for x-ray imaging applications," *IEEE Trans. Nucl. Sci.* **45**(3), 492–496 (1998).

¹¹ J. Stewart, "Techniques of integration," in *Calculus: Early Transcendentals*, 5th ed., edited by B. Pirtle, and S. Green (Brooks-Cole, Belmont, CA, 2003), Chap. 7, pp. 474–545.

¹² H. H. Barrett and K. J. Myers, "Energy transport and photons," in *Foundations of Image Science*, edited by B. E. A. Saleh (Wiley, New York, NY, 2004), Chap. 10, pp. 551–630.

¹³ H. H. Barrett and K. J. Myers, "Series expansions and integral transforms," in *Foundations of Image Science*, edited by B. E. A. Saleh (Wiley, New York, NY, 2004), Chap. 4, pp. 175–214.

¹⁴ B. Zhao and W. Zhao, "Three-dimensional linear system analysis for breast tomosynthesis," *Med. Phys.* **35**(12), 5219–5232 (2008).

¹⁵ T. Mertelmeier, J. Orman, W. Haerer, and M. K. Dudam, "Optimizing filtered backprojection reconstruction for a breast tomosynthesis prototype device," in *Physics of Medical Imaging*, edited by M. J. Flynn and J. Hsieh (SPIE, San Diego, 2006).

¹⁶ M. Albert and A. D. A. Maidment, "Linear response theory for detectors consisting of discrete arrays," *Med. Phys.* **27**(10), 2417–2434 (2000).

¹⁷ R. J. Acciavatti and A. D. A. Maidment, "An analytical model of NPS and DQE comparing photon counting and energy integrating detectors," in *SPIE Medical Imaging*, edited by E. Samei and N. J. Pelc (SPIE, San Diego, CA, 2010), pp. 76220I-1–76220I-12.

¹⁸ R. J. Acciavatti and A. D. A. Maidment, "A comparative analysis of OTF, NPS, and DQE in energy integrating and photon counting digital x-ray detectors," *Med. Phys.* **37**(12), 6480–6495 (2010).

¹⁹ A.-K. Carton, P. Bakic, C. Ullberg, and A. D. A. Maidment, "Development of a 3D high-resolution physical anthropomorphic breast phantom," in *Medical Imaging 2010: Physics of Medical Imaging*, edited by E. Samei and N. J. Pelc (SPIE, San Diego, CA, 2010), pp. 762206-1–762206-8.

²⁰ A.-K. Carton, P. Bakic, C. Ullberg, H. Derand, and A. D. A. Maidment, "Development of a physical 3D anthropomorphic breast phantom," *Med. Phys.* **38**(2), 891–896 (2011).

²¹ A. B. Wolbarst, "Resolution and magnification," in *Physics of Radiology*, 2nd ed. (Medical Physics, Madison, WI, 2005), Chap. 30, pp. 333–340.

²² J. Kuo, P. A. Ringer, S. G. Fallows, P. R. Bakic, A. D. A. Maidment, and S. Ng, "Dynamic reconstruction and rendering of 3D tomosynthesis images," in *SPIE Medical Imaging*, edited by N. J. Pelc, E. Samei, and R. M. Nishikawa (SPIE, Lake Buena Vista, FL, 2011), pp. 796116-1–796116-11.

²³ M. Albert, D. J. Beideck, P. R. Bakic, and A. D. A. Maidment, "Aliasing effects in digital images of line-pair phantoms," *Med. Phys.* **29**(8), 1716–1718 (2002).

²⁴ M. Lanyi, "Differential diagnosis of microcalcifications," in *Diagnosis and Differential Diagnosis of Breast Calcifications* (Springer-Verlag, Berlin, 1988), Chap. 7, pp. 193–231.

²⁵ P. R. Bakic, P. Ringer, J. Kuo, S. Ng, and A. D. A. Maidment, "Analysis of geometric accuracy in digital breast tomosynthesis reconstruction," *Lect. Notes Comput. Sci.* **6136**, 62–69 (2010).

²⁶ W. Que and J. A. Rowlands, "X-ray imaging using amorphous selenium: Inherent spatial resolution," *Med. Phys.* **22**(4), 365–374 (1995).

²⁷ G. Hajdok and I. A. Cunningham, "Penalty on the detective quantum efficiency from off-axis incident x rays," in *Medical Imaging 2004: Physics of Medical Imaging*, edited by M. J. Yaffe and M. J. Flynn (SPIE, San Diego, CA, 2004), pp. 109–118.

²⁸ J. G. Mainprize, A. K. Bloomquist, M. P. Kempston, and M. J. Yaffe, "Resolution at oblique incidence angles of a flat panel imager for breast tomosynthesis," *Med. Phys.* **33**(9), 3159–3164 (2006).

²⁹ R. J. Acciavatti and A. D. A. Maidment, "Calculation of OTF, NPS, and DQE for oblique x-ray incidence on turbid granular phosphors," *Lect. Notes Comput. Sci.* **6136**, 436–443 (2010).

³⁰ M. Freed, S. Park, and A. Badano, "A fast, angle-dependent, analytical model of CsI detector response for optimization of 3D x-ray breast imaging systems," *Med. Phys.* **37**(6), 2593–2605 (2010).

³¹ M. Freed, S. Park, and A. Badano, "Erratum: 'A fast, angle-dependent, analytical model of CsI detector response for optimization of 3D x-ray breast imaging systems'," [*Med. Phys.* **37**, 2593–2605 (2010)], *Med. Phys.* **38**(4), 2307 (2011).

³² A. Badano, M. Freed, and Y. Fang, "Oblique incidence effects in direct x-ray detectors: A first-order approximation using a physics-based analytical model," *Med. Phys.* **38**(4), 2095–2098 (2011).

³³ R. J. Acciavatti and A. D. A. Maidment, "Optimization of phosphor-based detector design for oblique x-ray incidence in digital breast tomosynthesis," *Med. Phys.* **38**(11), 6188–6202 (2011).

³⁴ P. C. Johns and M. J. Yaffe, "X-ray characterization of normal and neoplastic breast tissues," *Phys. Med. Biol.* **32**(6), 675–695 (1987).

³⁵ M. J. Yaffe, "Digital mammography," in *Handbook of Medical Imaging, Volume 1, Physics and Psychophysics*, edited by J. Beutel, H. L. Kundel and R. L. V. Metter (SPIE: The International Society for Optical Engineering, Bellingham, WA, 2000), Chap. 5, pp. 329–372.

³⁶ J. T. Bushberg, J. A. Seibert, M. Edwin, J. Leidholdt, and J. M. Boone, "Mammography," in *The Essential Physics of Medical Imaging*, 2nd ed., edited by J.-R. John, A. Snyder, and T. DeGeorge (Lippincott, Philadelphia, PA, 2002), Chap. 8, pp. 191–229.

³⁷ M. J. Berger *et al.*, XCOM: Photon Cross Sections Database (Available URL: <http://physics.nist.gov/xcom>).

- ³⁸H. E. Johns and J. R. Cunningham, "Diagnostic radiology," in *The Physics of Radiology*, 4th ed. (Thomas, Springfield, IL, 1983), Chap. 16, pp. 557–669.
- ³⁹B. Ren, C. Ruth, J. Stein, A. Smith, I. Shaw, and Z. Jing, "Design and performance of the prototype full field breast tomosynthesis system with selenium based flat panel detector," in *SPIE Medical Imaging*, edited by M. J. Flynn (SPIE, San Diego, CA, 2005), pp. 550–561.
- ⁴⁰E. Shaheen, N. Marshall, and H. Bosmans, "Investigation of the effect of tube motion in breast tomosynthesis: Continuous or step and shoot?" in *SPIE Medical Imaging*, edited by N. J. Pelc, E. Samei, and R. M. Nishikawa (SPIE, Lake Buena Vista, FL, 2011), pp. 79611E-1–79611E-9.
- ⁴¹R. J. Acciavatti and A. D. A. Maidment, "Optimization of continuous tube motion and step-and-shoot motion in digital breast tomosynthesis systems with patient motion," in *SPIE Medical Imaging*, edited by N. J. Pelc, R. M. Nishikawa, and B. R. Whiting (SPIE, San Diego, CA, 2012), pp. 831306-1–831306-12.
- ⁴²A. K. Bloomquist, M. J. Yaffe, G. E. Mawdsley, and D. M. Hunter, "Lag and ghosting in a clinical flat-panel selenium digital mammography system," *Med. Phys.* **33**(8), 2998–3005 (2006).
- ⁴³J. H. Siewerdsen and D. A. Jaffray, "A ghost story: Spatio-temporal response characteristics of an indirect-detection flat-panel imager," *Med. Phys.* **26**(8), 1624–1641 (1999).
- ⁴⁴W. Zhao, G. DeCrescenzo, S. O. Kasap, and J. A. Rowlands, "Ghosting caused by bulk charge trapping in direct conversion flat-panel detectors using amorphous selenium," *Med. Phys.* **32**(2), 488–500 (2005).
- ⁴⁵H. H. Barrett and K. J. Myers, "Noise in detectors," in *Foundations of Image Science*, edited by B. E. A. Saleh (Wiley, New York, NY, 2004), Chap. 12, pp. 701–800.
- ⁴⁶D. M. Tucker, G. T. Barnes, and D. P. Chakraborty, "Semiempirical model for generating tungsten target x-ray spectra," *Med. Phys.* **18**(2), 211–218 (1991).
- ⁴⁷J. M. Boone, T. R. Fewell, and R. J. Jennings, "Molybdenum, rhodium, and tungsten anode spectral models using interpolating polynomials with application to mammography," *Med. Phys.* **24**(12), 1863–1874 (1997).
- ⁴⁸M. M. Blough, R. G. Waggener, W. H. Payne, and J. A. Terry, "Calculated mammographic spectra confirmed with attenuation curves for molybdenum, rhodium, and tungsten targets," *Med. Phys.* **25**(9), 1605–1612 (1998).
- ⁴⁹P. R. Bakic, C. Zhang, and A. D. A. Maidment, "Development and characterization of an anthropomorphic breast software phantom based upon region-growing algorithm," *Med. Phys.* **38**(6), 3165–3176 (2011).
- ⁵⁰J. Stewart, "Multiple integrals," in *Calculus: Early Transcendentals*, 5th ed., edited by B. Pirtle and S. Green (Brooks-Cole, Belmont, CA, 2003), Chap. 15, pp. 980–1053.